A&A 572, A57 (2014)
DOI: 10.1051/0004-6361/201423924

Astronomy & Astrophysics

The white dwarf's carbon fraction as a secondary parameter of Type Ia supernovae⋆

Sebastian T. Ohlmann[1], Markus Kromer[2,3], Michael Fink[1], Rüdiger Pakmor[4], Ivo R. Seitenzahl[1,3,6,7], Stuart A. Sim[5,6,7], and Friedrich K. Röpke[1]

[1] Institut für Theoretische Physik und Astrophysik, Universität Würzburg, Emil-Fischer-Str. 31, 97074 Würzburg, Germany
e-mail: sohlmann@astro.uni-wuerzburg.de
[2] The Oskar Klein Centre & Department of Astronomy, Stockholm University, AlbaNova, 106 91 Stockholm, Sweden
[3] Max-Planck-Institut für Astrophysik, Karl-Schwarzschild-Str. 1, 85741 Garching, Germany
[4] Heidelberger Institut für Theoretische Studien, Schloss-Wolfsbrunnenweg 35, 69118 Heidelberg, Germany
[5] Astrophysics Research Centre, School of Mathematics and Physics, Queen's University Belfast, Belfast BT7 1NN, UK
[6] Research School of Astronomy and Astrophysics, Mount Stromlo Observatory, Cotter Road, Weston Creek, ACT 2611, Australia
[7] ARC Centre of Excellence for All-sky Astrophysics (CAASTRO)

Received 1 April 2014 / Accepted 1 September 2014

ABSTRACT

Context. Binary stellar evolution calculations predict that Chandrasekhar-mass carbon/oxygen white dwarfs (WDs) show a radially varying profile for the composition with a carbon depleted core. Many recent multi-dimensional simulations of Type Ia supernovae (SNe Ia), however, assume the progenitor WD has a homogeneous chemical composition.
Aims. In this work, we explore the impact of different initial carbon profiles of the progenitor WD on the explosion phase and on synthetic observables in the Chandrasekhar-mass delayed detonation model. Spectra and light curves are compared to observations to judge the validity of the model.
Methods. The explosion phase is simulated using the finite volume supernova code Leafs, which is extended to treat different compositions of the progenitor WD. The synthetic observables are computed with the Monte Carlo radiative transfer code Artis.
Results. Differences in binding energies of carbon and oxygen lead to a lower nuclear energy release for carbon depleted material; thus, the burning fronts that develop are weaker and the total nuclear energy release is smaller. For otherwise identical conditions, carbon depleted models produce less ^{56}Ni. Comparing different models with similar ^{56}Ni yields shows lower kinetic energies in the ejecta for carbon depleted models, but only small differences in velocity distributions and line velocities in spectra. The light curve width-luminosity relation (WLR) obtained for models with differing carbon depletion is roughly perpendicular to the observed WLR, hence the carbon mass fraction is probably only a secondary parameter in the family of SNe Ia.

Key words. supernovae: general – hydrodynamics – nuclear reactions, nucleosynthesis, abundances – radiative transfer – binaries: close – white dwarfs

1. Introduction

Despite enormous efforts in recent years, both in observation and modeling, identification of the progenitors of Type Ia supernovae (SNe Ia) remains elusive; no system has been observed so far (e.g., Roelofs et al. 2008; Li et al. 2011) and model predictions do not allow us to unambiguously distinguish different progenitor scenarios (e.g., Röpke et al. 2012). It is generally agreed that SNe Ia result from thermonuclear explosions of carbon/oxygen white dwarfs (WDs) in interacting binary systems, where mass transfer from the secondary component triggers the explosion (e.g., Hillebrandt & Niemeyer 2000). Depending on whether the secondary star is degenerate, the systems are distinguished in single degenerate (SD) systems – with main sequence, red giant, or sdB companion stars, for example – and double degenerate (DD) systems – with He or carbon/oxygen (C/O) WDs as secondary components. For a review of explosion models see Hillebrandt & Niemeyer (2000); more recent explosion models and their comparison to observations are presented in Hillebrandt et al. (2013). Interestingly, for the subclass of SN 2002cx-like SNe, pure deflagrations of Chandrasekhar-mass (Chandrasekhar 1931) WDs (Jordan et al. 2012b; Kromer et al. 2013; Fink et al. 2014) in the SD channel match observables quite well (Kromer et al. 2013). For normal SNe Ia, the most promising candidates are delayed detonations of Chandrasekhar-mass WDs in SD systems (e.g., Golombek & Niemeyer 2005; Gamezo et al. 2005; Röpke & Niemeyer 2007; Bravo & García-Senz 2008; Jordan et al. 2008; Townsley et al. 2009; Bravo & García-Senz 2009; Bravo et al. 2009; Jackson et al. 2010; Seitenzahl et al. 2011; Röpke et al. 2012; Jordan et al. 2012a; Seitenzahl et al. 2013; Sim et al. 2013), double detonations of sub-Chandrasekhar-mass WDs in SD and DD systems (e.g., Fink et al. 2007, 2010; Moll & Woosley 2013), and violent mergers of sub-Chandrasekhar-mass WDs in DD systems (e.g., Pakmor et al. 2012a,b, 2013; Moll et al. 2014; Raskin et al. 2014). A recent comparison to SN 2011fe (Röpke et al. 2012) shows that disentangling different models is hard given the current predictions in the optical regime. Other suggestions for progenitor scenarios include head-on collisions (e.g., Rosswog et al. 2009; Raskin et al. 2009; Kushnir et al. 2013; García-Senz et al. 2013) and the core-degenerate scenario (e.g., Soker et al. 2014).

⋆ Tables 3 and 4 are available in electronic form at http://www.aanda.org

The level of interest in SNe Ia has risen in the past 20 years mainly because they can be used as distance indicators in cosmology (for a review, see Leibundgut 2008), leading to the discovery of an accelerated expansion of the Universe (e.g., Riess et al. 1998; Schmidt et al. 1998; Perlmutter et al. 1999). The foundation for this development was the establishment of a light curve width-luminosity relation (WLR, also called the Phillips relation) by Phillips (1993, see also the earlier work of Pskovskii 1977). This relation enables the estimation of absolute luminosities from the light curve width: broader light curves correspond to brighter SNe. Thus, to a first approximation, SNe Ia are a one-parameter family driven by the primary parameter which affects light curve width and luminosity in such a way that the observed WLR emerges. As observed SNe Ia show some scatter around this WLR, some secondary parameters have to be present influencing light curve width and luminosity following a relation different from the mean observed WLR. One challenge present in SN Ia models is identifying the primary and secondary physical parameters (or sets of parameters) to better understand the physical origin of this relation. This should, as an ultimate goal, lead to a theoretical examination and justification of using this relation for a wide range of parameters, such as redshift or host stellar population.

In the multi-dimensional simulations presented here, we investigate the delayed detonation model in Chandrasekhar-mass WDs (Blinnikov & Khokhlov 1986; Khokhlov 1991a). If Chandrasekhar mass models are to account for normal SNe Ia (in the sense of Branch et al. 1993), the combination of a deflagration and a detonation is needed: neither pure detonation nor pure deflagration is sufficient. Pure detonations of Chandrasekhar-mass WDs produce almost no intermediate mass elements (IME) because of the high densities ($\gtrsim 10^7$ g cm^{-3} in most of the WD; Arnett et al. 1971, see also introduction in Khokhlov 1991a). Pure deflagrations have recently been identified as promising models for 2002cx-like SNe Ia (Jordan et al. 2012b; Kromer et al. 2013), but in other parameter ranges they fail to reproduce SNe Ia (Fink et al. 2014; Ma et al. 2013; Röpke 2008). The densities through which the detonation propagates have to be lowered to produce more IME. Hence, a deflagration flame first burns from the core outwards to the surface, thereby expanding the WD before the detonation is initiated. The mechanism of igniting the detonation is unclear, but several possibilities are proposed and explored in 3D simulations: the spontaneous deflagration-to-detonation transition (spontaneous DDT, Gamezo et al. 2005; Röpke & Niemeyer 2007; Bravo & García-Senz 2008; Townsley et al. 2009; Jackson et al. 2010; Seitenzahl et al. 2011; Röpke et al. 2012; Seitenzahl et al. 2013; Sim et al. 2013), the gravitationally confined detonation (GCD, Jordan et al. 2008, 2012a), and the pulsational reverse detonation (PRD, Bravo & García-Senz 2009; Bravo et al. 2009). These models differ in the way the detonation is initiated. The detonation emerges only in the spontaneous DDT from regions where the flame turbulently mixes fuel with ashes; in the other models, the deflagration initiates a large-scale motion of gas, leading at some point to highly compressed hot spots, where the detonation is initiated. Thus, these models also differ in the hydrodynamical structure at the onset of the detonation.

It is often assumed that for these models, the primary parameter of the WLR may be the ignition configuration, i.e., the shape of the initial deflagration flame (e.g., Seitenzahl et al. 2013). This parameter indeed leads to a variety of ^{56}Ni masses and hence luminosities, but fails to reproduce the WLR in the recent study of Sim et al. (2013, although Kasen et al. 2009 find their 2D models populate a similar region to that of the WLR by changing ignition configuration and DDT criterion). Thus, recent multi-dimensional spontaneous DDT models (Sim et al. 2013; Seitenzahl et al. 2013; Röpke et al. 2012) show reasonable agreement to observations, but some shortcomings remain, such as colors that are too red at maximum, velocities that are too high, and a failure to explain the observed WLR in terms of a sequence of models with differing initial deflagration strengths. Therefore, it is vital to examine the consequences of other parameters. For the single degenerate scenario considered here, the initial carbon fraction is one parameter that is expected to show variations for different progenitor systems depending on the zero-age main sequence (ZAMS) mass and on the metallicity of the progenitor star (Umeda et al. 1999b; Domínguez et al. 2001). It affects important parameters of the light curve evolution, such as the kinetic energy of the ejecta. In 1D model studies, this has already been examined by Höflich et al. (1998) and Umeda et al. (1999a); Höflich et al. (2010) also suggest the C fraction to be a secondary parameter.

The main objective of this work is to examine if varying the initial C fraction resolves any of the discrepancies between predictions of the spontaneous DDT model and observations of normal SNe Ia. More specifically, we want to answer the following two questions:

(i) How does the carbon mass fraction affect the width-luminosity relation predicted for our 3D models? In particular, does it drive variations along the observed Phillips relation of SNe Ia?
(ii) Does a reduction of the carbon fraction result in better agreement of spectral features?

To this end, we examine the impact of different initial compositions on the explosion process in multi-dimensional DDT models including its interplay with other parameters and present detailed nucleosynthesis results and synthetic light curves and spectra. First, we give an overview of initial parameters involved in spontaneous DDT models in Sect. 2. In Sect. 3, we explain our numerical methods: the initial WD models, the hydrodynamic modeling of the explosion phase, the detailed nucleosynthesis calculations, and the radiative transfer simulations. In Sect. 4, we examine the hydrodynamic evolution in a parameter study of 2D simulations as well as for a few 3D simulations and present detailed nucleosynthesis results. Results from radiative transfer simulations, synthetic light curves and spectra, for a series of 3D simulations are presented in Sect. 5 along with a discussion of the width-luminosity relation. We conclude in Sect. 6 with answers to the questions posed above.

2. Initial parameters of delayed detonation models for SNe Ia

The hydrodynamic evolution of the explosion phase in spontaneous DDT models is governed by several parameters. In some cases, these are poorly constrained and in others, they are constrained to vary in a certain range.

In this work, we systematically explore the initial carbon fraction of the pre-explosion WD, which depends on the evolution of the system. In the phase prior to explosion, simmering sets in, changing the composition in the interior. This has been modeled (e.g., Lesaffre et al. 2006), but it is still difficult to include important effects such as the URCA process (Lesaffre et al. 2005, 2006). Nevertheless, these calculations show that the progenitor WD is composed of an outer layer of accreted material with an equal-by-mass composition of C and O, and an inner

convective core with a lower C mass fraction. According to the calculations of Lesaffre et al. (2006), this mass fraction and the size of the convective core is correlated to other parameters, such as the central density or metallicity. The central C mass fraction depends on the ZAMS mass and the metallicity of the progenitor (Umeda et al. 1999b; Domínguez et al. 2001). The range in the central C fraction is about 0.24 to 0.37 for the models of Umeda et al. (1999b) and about 0.21 to 0.32 for the models of Domínguez et al. (2001). However, because of limitations in the modeling and in the nuclear data, the central C concentration is rather uncertain and Domínguez et al. (2001) suggest that it may vary between 0.1 and 0.5. The chemical stratification also changes during the simmering phase prior to ignition; therefore, we choose our model parameters similar to the models of Lesaffre et al. (2006). We account for the possible spread in central C fractions by varying it between 0.2 and 0.5 in our models. The effect of the initial composition on the explosion is mainly by a different nuclear energy release in the burning: owing to the lower binding energy of C compared to O, material with less C possesses a smaller energy difference to the burning products, which are mostly in the iron group.

Changing the initial metallicity of the WD progenitor mainly influences the nucleosynthesis, since the principal influcence on the hydrodynamic evolution is due to the dependence of the equation of state on the electron fraction. In the nucleosynthesis, a lower metallicity and thus higher electron fraction leads to a larger ^{56}Ni production (Timmes et al. 2003; Travaglio et al. 2005; Seitenzahl et al. 2013) owing to reduced neutronization, but the effect is not large enough for a primary parameter.

The initial evolution of the deflagration flame is governed by the ignition configuration, which is poorly understood. Hydrodynamical simulations (Höflich & Stein 2002; Kuhlen et al. 2006; Zingale et al. 2009) favor a dipole structure of the convective flow preceding ignition, which may be fractured by rotation, yielding ignition over a broader region. In our simulations, we place a certain number of ignition kernels near the center of the WD to excite different numerical modes of the deflagration flame. The number of these kernels determines the strength of the deflagration, i.e., the rate of energy production (Seitenzahl et al. 2013; Fink et al. 2014). More ignition kernels corresponds to a stronger deflagration and thus to a stronger expansion of the WD. Consequently, lower densities result at the onset of the detonation and thus, less ^{56}Ni is produced. The range in deflagration strengths studied in Seitenzahl et al. (2013) is able to reproduce the observed range in brightnesses of normal SNe Ia, but fails to explain the WLR (Sim et al. 2013). This study implies that the deflagration strength is probably not the primary parameter.

Another important factor in the hydrodynamic evolution is the DDT criterion. Although it is still unknown if and how this transition is realized in SNe Ia, some restrictions on the mechanism have been placed. The proposed instant of DDT to occur is when the flame leaves the flamelet regime and enters the distributed burning regime (Woosley et al. 2009), where hot ashes and cold fuel mix in the presence of large turbulent velocity fluctuations; hot spots result and a detonation is initiated. Woosley (2007) estimate the density of the DDT to lie in the range of $(0.5{-}1.5) \times 10^7$ g cm^{-3}. The higher the density at the DDT is, the more ^{56}Ni is produced (see the 2D simulations by Kasen et al. 2009). In the 3D simulations by Seitenzahl et al. (2013), the DDT criterion was fixed for all simulations in order to examine the consequences of different ignition conditions. It is unclear why the DDT criterion should change in different SNe, if it is the primary parameter.

The central density of the WD at ignition is on the order of 10^9 g cm^{-3}. However, some variation is possible, as the mass of a near-Chandrasekhar-mass WD is almost independent of the central density; this depends on the pre-explosion evolution. Higher initial densities shift the explosion products to more neutron-rich nuclei, mostly stable iron group elements (IGE) instead of ^{56}Ni. In their parameter study with 2D simulations, Krueger et al. (2010) find that a higher central density leads to similar overall production of IGE; but a lower amount of ^{56}Ni is produced, as more neutron-rich nuclei are formed. Seitenzahl et al. (2011), in contrast, find in their 3D simulations a higher IGE production for higher central densities, whereas the amount of ^{56}Ni is roughly constant. In any case, this effect is too small to be a primary parameter.

3. Numerical methods

To compute synthetic observables from explosion models, we use a modeling pipeline: after creating the initial WD models, the explosion phase is simulated using the hydrodynamic code Leafs; then, detailed nucleosynthesis results are computed in a postprocessing step; finally, synthetic observables are obtained with the radiative transfer Monte Carlo code Artis, using mapped data from the previous steps.

3.1. Initial WD models

The initial WD models have been created as cold isothermal WDs by integrating the hydrostatic equilibrium equations for a central density of 2.9×10^9 g cm^{-3} and a constant temperature of 5×10^5 K. The equation of state used for the integration is the same as in Leafs. The composition of the WD is chosen based on the results of Lesaffre et al. (2006): uniform composition in the convective core and in the outer accretion layer with a smoothly connecting transition region. In the outer accretion layer, $X(^{12}\mathrm{C}) = 0.5$, whereas in the convective core $X(^{12}\mathrm{C})$ ranges from 0.2 to 0.5, depending on the model. The convective core ends at about 1 $M_\odot$ and the accretion layer starts at 1.2 $M_\odot$; again these values correspond to a typical scenario from Lesaffre et al. (2006). The size of the convective core depends on the chosen ignition criterion and for a certain choice of parameters, its mass is about 1 $M_\odot$ for a central density of 2.9×10^9 g cm^{-3} (compare solid lines in Fig. 7 of Lesaffre et al. 2006). We fix the mass of the convective core for all models and vary only the C fraction in order to have only one parameter changing in our models. Moreover, we take a rather wide range of the C fraction from 0.2 to 0.5 to assess the maximum possible influence of this parameter on the explosion process and on observables. Other findings indicate that the mass of the convective core may vary in a rather wide range, depending on variables such as the chemical stratification (Piro & Chang 2008) and uncertainties in the nuclear reaction rate data (Bravo et al. 2011). Moreover, in the models of Bravo et al. (2011), a C depleted core develops in the innermost 0.05 $M_\odot$ of the WD. This should not influence the evolution of the flame much because the evolution of the flame in our 3D models is mostly governed by the Rayleigh-Taylor instabilities at later times. Thus, a C depletion in the very core should not significantly change the hydrodynamical evolution and thus also not the resulting observables.

To clarify the composition of each model, we introduce a naming scheme. The first part of the model names encodes the initial composition: cXY denotes a homogeneous progenitor model with a carbon mass fraction of XY%. Additional more realistic progenitor models (following Lesaffre et al. 2006) are

labeled rpcXY corresponding to a homogeneous carbon depleted core with a carbon mass fraction of XY%.

3.2. Hydrodynamic simulations

We use the supernova code LEAFS (Reinecke et al. 1999, 2002) for the hydrodynamic simulations of the explosion phase. It employs a finite-volume, grid-based scheme in a Eulerian formulation of the piecewise parabolic method by Colella & Woodward (1984), in the PROMETHEUS implementation by Fryxell et al. (1989). The Riemann solver is implemented according to Colella & Glaz (1985), being capable of using a general convex equation of state. The equation of state is based on the Timmes equation of state (Timmes & Swesty 2000).

Thermonuclear flames are modeled with the levelset method (Osher & Sethian 1988) as described by Reinecke et al. (1999, 2002). This approach approximates the flame front as a discontinuity, which burns the nuclear fuel instantaneously. The large difference in scales of several orders of magnitude between the flame width (~mm-cm) and the grid cell size (~km) justifies this approximation. Nuclear burning is treated in an approximate scheme, yielding the final composition directly behind the front. To track the energy release, a simplified composition is used including five pseudo-species, α particles, ^{12}C, ^{16}O, "Mg" (representing IME) and "Ni" (representing iron group elements, IGE); these approximate fuel and burning products from the different burning stages. Nuclear statistical equilibrium (NSE) is treated approximately by adjusting the mass fractions of IGE and α particles to follow the energy release depending on density and temperature. The detailed nucleosynthetic yields are computed in a postprocessing step using the method of tracer particles (see Sect. 3.3). The tables giving the composition behind the level set depend on the density and composition of the unburnt fuel and have to be calculated once, prior to the simulations. This is done using an iterative calibration method similar to Fink et al. (2010). The method is extended to different initial compositions to allow for varying compositions (for further details, see Appendix A).

For the computational grid, we use the moving hybrid grid technique as described in Röpke et al. (2006b). An inner equidistant grid tracks the deflagration flame and expands into the outer, exponentially spaced grid as the deflagration evolves to allow for high resolution in the beginning. The deflagration burning takes place in the flamelet regime of turbulent combustion. The effects of turbulence on unresolved scales are accounted for by a subgrid-scale model, which is used to compute turbulent velocity fluctuations below the grid scale. For 2D models, the subgrid-scale model by Niemeyer & Hillebrandt (1995) is used, whereas for 3D models, a more elaborate model is employed as introduced by Schmidt et al. (2006a,b).

The deflagration-to-detonation transition (DDT) is assumed to occur when the turbulent burning changes from the flamelet regime to the distributed burning regime (Woosley et al. 2009). Here, the internal flame structure is disturbed by turbulent eddies due to an increased flame width at lower densities. This leads to heat transfer from hot ashes to cold fuel (Niemeyer & Woosley 1997; Woosley 2007), whereupon hot spots may form potentially initiating a detonation via the Zel'dovich gradient mechanism (Zel'dovich et al. 1970). The flame widths necessary for this transition are reached in a density range of $(0.5-1.5)\times10^7$ g cm^{-3} (Woosley 2007). Furthermore, high turbulent velocity fluctuations of the order of 10^8 cm s^{-1} must be present at the flame front (Lisewski et al. 2000; Woosley et al. 2009), which was found in 3D deflagration models by Röpke (2007). For our 2D models, the DDT criterion is modeled as in Kasen et al. (2009), but with differing parameters. A detonation is initiated in a cell if the density lies in a certain range and if the Karlovitz number Ka is larger than a given minimum value. Since Ka $\propto (u')^{3/2}$ (Kasen et al. 2009, Supp. Information), where u' denotes the turbulent velocity fluctuations below the grid scale, this criterion requires the turbulent velocity fluctuations to be above a certain threshold. In three dimensions, the DDT criterion is modeled as described in Ciaraldi-Schoolmann et al. (2013), but varying the parameters. In this criterion, an effective flame surface is calculated by choosing cells in a certain density and fuel mass fraction range. This surface is additionally multiplied by the probability of large velocity fluctuations being present and it is required to exceed a critical value for at least half an eddy turnover time to ensure sufficient mixing between fuel and ashes.

Table 1. Parameters for DDT criteria for 2D models similar to Kasen et al. (2009).

Criterion	$\rho_{\rm min}$	$\rho_{\rm max}$	Ka$_{\rm min}$
ddt1	0.6	1.2	250
ddt2	0.5	0.8	1000
ddt3	0.5	0.8	2250
ddt4	0.6	1.2	2250

Notes. For details on the different parameters see Kasen et al. (2009), supplementary information. The densities are given in 10^7 g cm^{-3}.

For the 2D simulations, a grid size of 512×1024 cells in axial symmetry was chosen, corresponding to a spatial resolution of 1.06 km in the inner part at the beginning of the simulation. The 3D simulations are full star simulations and use a grid with 512^3 cells, which corresponds to a spatial resolution of 2.14 km in the inner part at the beginning of the simulation.

The model names for 2D models consist of three parts; the first part gives the initial composition, as explained above. The second part of the model name consists of the DDT criterion; the corresponding parameters are given in Table 1 and are similar to those used by Kasen et al. (2009). The last part of the model name is determined by the initial conditions, the number gives the number of initial ignition spots for the deflagration flame. The DDT criteria and ignition conditions are the same as in Kasen et al. (2009) with slightly different notations. The parameter study comprises of runs for five different initial composition profiles (c20, c30, c40, c50, and rpc32), for eight different ignition configurations (dd020, dd050, dd060, dd080, dd090, dd100, dd100C, and dd150), and for two different DDT criteria (ddt1, ddt2). The rpc32 model has been run for all four DDT criteria of Table 1.

For the 3D models, the treatment of initial composition is the same as for the 2D models (see above). The values used for the limits in the DDT criterion are $0.4 < X_{\rm fuel} < 0.6$ and $0.6 < \rho/(10^7\ {\rm g\ cm^{-3}}) < 0.9$ (for details, see Ciaraldi-Schoolmann et al. 2013) , where $X_{\rm fuel}$ is the mass fraction of unburnt material in the cell. The parameter range around 0.5 ensures that a detonation is ignited only in cells where fuel and ashes are mixed. This criterion for the 3D models is termed DDT8 and differs from the one used by Seitenzahl et al. (2013). The ignition conditions for the deflagration flame are the same as described by Seitenzahl et al. (2013).

3.3. Nucleosynthetic postprocessing

Since coupling a reaction network to the hydrodynamic equations is computationally very expensive, we compute

the detailed nucleosynthetic abundances in an additional postprocessing step. This was first done by Thielemann et al. (1986) for 1D models, computing a nuclear reaction network for the Lagrangian mass shells. For multi-dimensional simulations, we use the concept of tracer particles, first introduced by Nagataki et al. (1997) in the context of Type II supernovae. In this method, tracer particles are passively advected with the flow and their thermodynamic trajectories are recorded. As the particles are moving in a Lagrangian manner, the nucleosynthetic abundances can be computed by evolving the nuclear network separately on each particle trajectory. The tracer particle method employed in our work is based on Travaglio et al. (2004) and uses the network of Thielemann et al. (1996) and Iwamoto et al. (1999) including 384 isotopes. More details on the algorithm can be found in Röpke et al. (2006a).

The distribution of the tracer particles is chosen according to Seitenzahl et al. (2010), who proposed variable tracer masses in order to improve the resolution in the outer layers with lower densities. The exact number of tracer particles depends on the simulation according to the algorithm by Seitenzahl et al. (2010) and is about 41 000 for 2D simulations and about 10^6 for 3D simulations.

The initial composition for the postprocessing is assumed to include the detailed solar metallicity of Asplund et al. (2009). The CNO cycle elements are assumed to be processed to ^{22}Ne during He burning; thus, their abundances are added by number to the ^{22}Ne abundance.

3.4. Radiative transfer simulations

The input data for the radiative transfer simulations is generated in the following way: the detailed nucleosynthesis data from the tracer particles is mapped onto a 200^3 Cartesian grid using an SPH-like algorithm; the density distribution is mapped on this grid from the hydrodynamic simulation. A further downsampling to a 50^3 grid yields the final input data for the radiative transfer calculation (more details in Kromer et al. 2010). The radiative transfer simulations are then carried out with the multi-dimensional Monte Carlo code Artis (Sim 2007; Kromer & Sim 2009). On a co-expanding grid, following the homologous expansion of the ejecta, 10^8 photon packages are propagated for 111 logarithmically spaced time steps from 2 d to 120 d after explosion. The computations are sped up in the beginning by using a gray approximation in optically thick cells (as discussed in Kromer & Sim 2009) and by assuming local thermodynamic equilibrium for the first 10 time steps, i.e., for the first two to three days post explosion. The atomic lines are taken from the same atomic data set as described in Gall et al. (2012), including approximately 2×10^6 bound-bound transitions. For the model N100 of Seitenzahl et al. (2013) and Sim et al. (2013), the radiative transfer simulations have been recomputed with this large atomic data set.

4. Hydrodynamic evolution and nucleosynthesis

In this section, we present the results from the hydrodynamic simulations of the explosion phase and detailed nucleosynthetic abundances. This is first done for a set of 2D simulations, which can be run in larger numbers (compared to 3D simulations), owing to the lower computational effort. Then, the results for a few 3D simulations are presented.

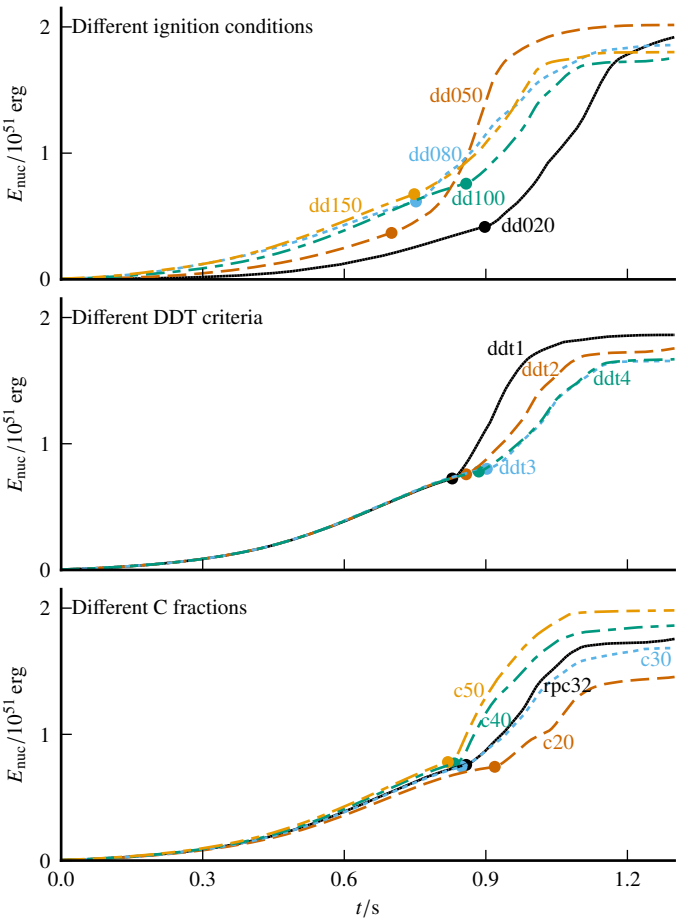

Fig. 1. Evolution of nuclear energy release vs. time for several 2D simulations. The dot marks the point of the first DDT. The *upper panel* shows simulations with different ignition conditions, but same initial composition and DDT criterion (rpc32_ddt2_ddxxx). The *middle panel* shows simulations with different DDT criteria, but same initial composition and ignition conditions (rpc32_ddtx_dd03). The *lower panel* shows simulations with different C mass fraction, but same DDT criterion and ignition conditions (xxx_ddt2_dd03).

4.1. Parameter study: 2D simulations

A parameter study was performed in two dimensions to explore the impact of different initial compositions. To this end, hydrodynamical simulations of DDT models, followed by nucleosynthetic postprocessing, were performed for a set of five different initial compositions for a range of different ignition conditions and different DDT criteria. This also allows us to examine the effects of ignition conditions and DDT criteria separately and to compare these to the repercussions of the initial composition. Moreover, our parameter study results in models with similar ^{56}Ni yields and thus similar luminosities; these may then be compared as models for the same supernova.

The repercussions of changing ignition conditions, DDT criteria, and initial compositions separately can be seen in Fig. 1. In the upper panel, different ignition configurations are compared. The nuclear energy release in the deflagration phase (prior to the first DDT marked with a dot) approximately increases with increasing number of ignition kernels. In this way, we can numerically excite varying deflagration strengths by changing the number of ignition kernels in our models. As the nuclear energy release is an indicator of the expansion of the WD, the WD has expanded more at the onset of the detonation for stronger

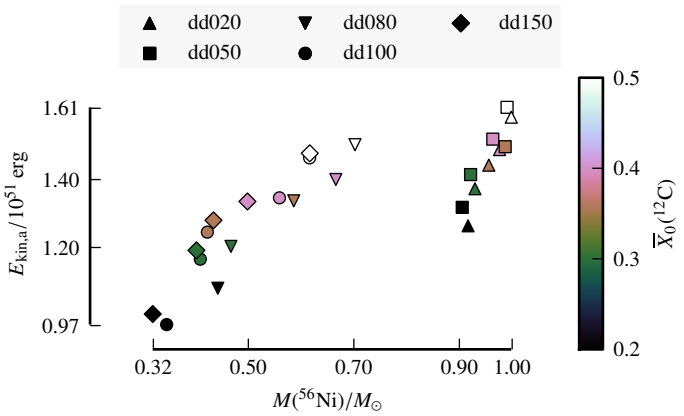

Fig. 2. Final asymptotic kinetic energy over total ^{56}Ni mass for several 2D models. Different ignition configurations are shown with different markers. The average carbon mass fraction at the beginning of the simulation is color-coded. The DDT criterion is ddt2 for all models.

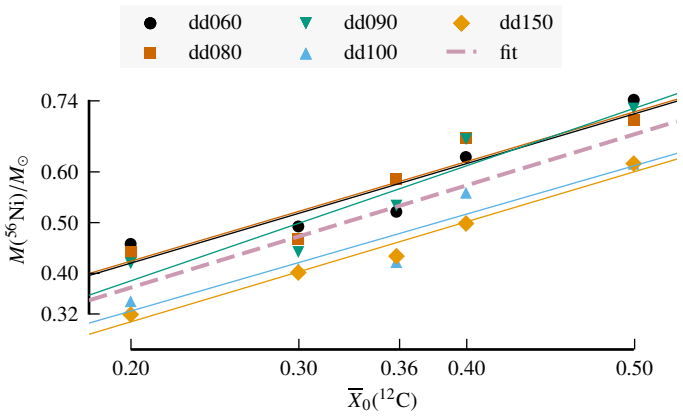

Fig. 3. Total ^{56}Ni mass over mean C mass fraction for several 2D models with different ignition conditions. The full lines show linear regressions for each ignition condition series; the dashed line shows the mean of all regressions.

deflagrations. Hence, for more ignition spots, the ensuing detonation burns less material at high densities; consequently, less ^{56}Ni is produced and less nuclear energy is released in total (see also Mazzali et al. 2007; Röpke & Niemeyer 2007; Seitenzahl et al. 2013; Fink et al. 2014). This relation, however, is fulfilled only approximately since the hydrodynamic evolution is highly non-linear and also depends on the locations of the ignition spots, not only on their number.

Changing the DDT criterion for otherwise identical conditions (Fig. 1, middle panel) leads to a different delay until the detonation is ignited. Later ignitions cause a lower ^{56}Ni production and also a lower release of nuclear energy in total because of the longer-lasting pre-expansion.

The repercussions of the initial composition on the hydrodynamic evolution for identical ignition configurations and DDT criteria can be seen in the lower panel of Fig. 1. The homogeneous models show a slightly lower nuclear energy release in the deflagration phase for lower carbon mass fractions which can be explained by the lower energy release of deflagration fronts at lower carbon mass fractions (see Appendix A). This leads to a slower expansion and the turbulent velocity fluctuations needed for the DDT develop more slowly; thus, the detonation is initiated later. This corresponds to a larger pre-expansion for lower carbon mass fractions. Hence less ^{56}Ni is produced and less nuclear energy is released in total. The more realistic model with a C depleted core (rpc32 model) is very similar to the homogeneous model with 30% C in the deflagration phase because the deflagration flame does not leave the C depleted core. In the detonation phase, however, a larger nuclear energy release can be seen, which is due to the detonation burning also in the outer layers with larger C mass fractions.

The nuclear energy release during the explosion phase drives the gravitational unbinding and the expansion of the ejecta; thus, the final, asymptotic kinetic energy of the ejecta is given by the sum of the initial internal energy, the initial gravitational energy (being negative) and the nuclear binding energy difference. This energy determines the scaling of the ejecta distribution in velocity space. The asymptotic kinetic energies and ^{56}Ni yields are compared for several models in Fig. 2. First, models with larger ^{56}Ni production show larger kinetic energies, which can be explained by the larger nuclear energy release. Second, when comparing models with identical ignition conditions but different initial compositions, a larger carbon mass fraction leads to a larger ^{56}Ni yield and a larger asymptotic kinetic energy. The ^{56}Ni masses for a model series with different initial compositions enclose a smaller interval for larger ^{56}Ni masses because the detonation burns mostly at high densities, where the influence of the composition is small (see Appendix A).

One important consequence is simply that different initial compositions lead to a spread in ^{56}Ni masses for identical ignition conditions. The relation between the total ^{56}Ni mass and the average initial C mass fraction $\overline{X}_0(^{12}\mathrm{C})$ is nearly linear (Fig. 3). Linear regressions for all model series with ^{56}Ni mass in the range for normal SNe Ia (~0.3–0.8 $M_\odot$) show correlation coefficients >0.94. Averaging over these regressions yields an approximate expression for the ^{56}Ni mass,

$$M\left(^{56}\mathrm{Ni}\right)/M_\odot = 0.17 + 1.01\overline{X}_0\left(^{12}\mathrm{C}\right), \quad (1)$$

for $0.2 < \overline{X}_0(^{12}\mathrm{C}) < 0.5$, showing a surprisingly simple mean relation between the initial C fraction and the ^{56}Ni mass.

If two different models are compared to the same SN, the models must produce a similar amount of ^{56}Ni to show a similar luminosity. This can be reached by varying initial composition, ignition conditions, and DDT criterion at once. As can be seen in Fig. 2, the model with the smaller C mass fraction produces similar ^{56}Ni yields for lower asymptotic kinetic energies than the model with the larger C mass fraction. Hence, the ejecta are distributed in a different way; and the light curves and spectra determined by this distribution will change.

The ejecta distribution in velocity space is shown for three models with similar ^{56}Ni masses but different initial compositions in Figs. 4–6.

The density structure (left panel) shows similar features for all three models: a higher density in the interior part ($\lesssim 10^4$ km s^{-1}), where most deflagration ashes reside alongside detonation ashes; and shocks in the outer parts, where multiple detonation fronts merged. The abundance structure (right panels) shows the same general features for all models: the central deflagration ashes are surrounded by layered detonation ashes. The models, however, also show differences: in the interior part ($\lesssim 10^4$ km s^{-1}), the variations are mostly due to the different hydrodynamic evolution of the deflagration flame for the different ignition conditions, but in the outer part, the ejecta are shifted to lower velocities for lower C mass fractions. Especially ^{56}Ni and stable iron isotopes are confined to lower velocities; also the peak of the ^{28}Si distribution shifts to lower velocities.

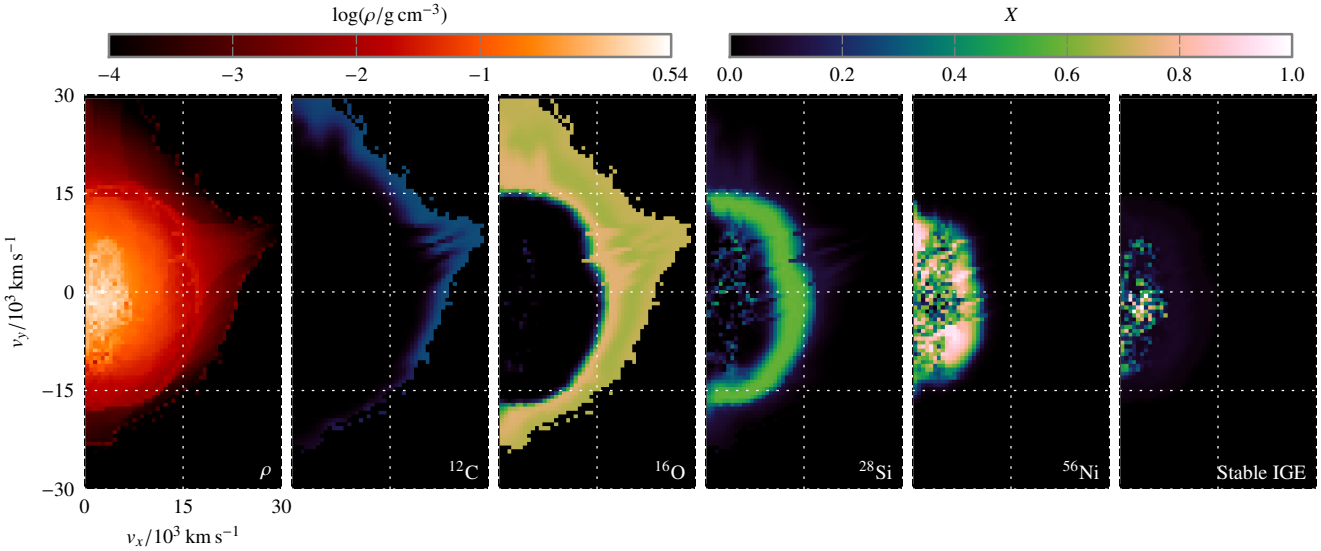

Fig. 4. Ejecta distribution after 100 s in velocity space for the 2D model c30_ddt1_dd150 producing 0.59 $M_\odot$ of ^{56}Ni. Shown are the density (*left panels*) and mass fractions (*right panels*, stable IGE are all iron group elements with $Z > 20$ without ^{56}Ni).

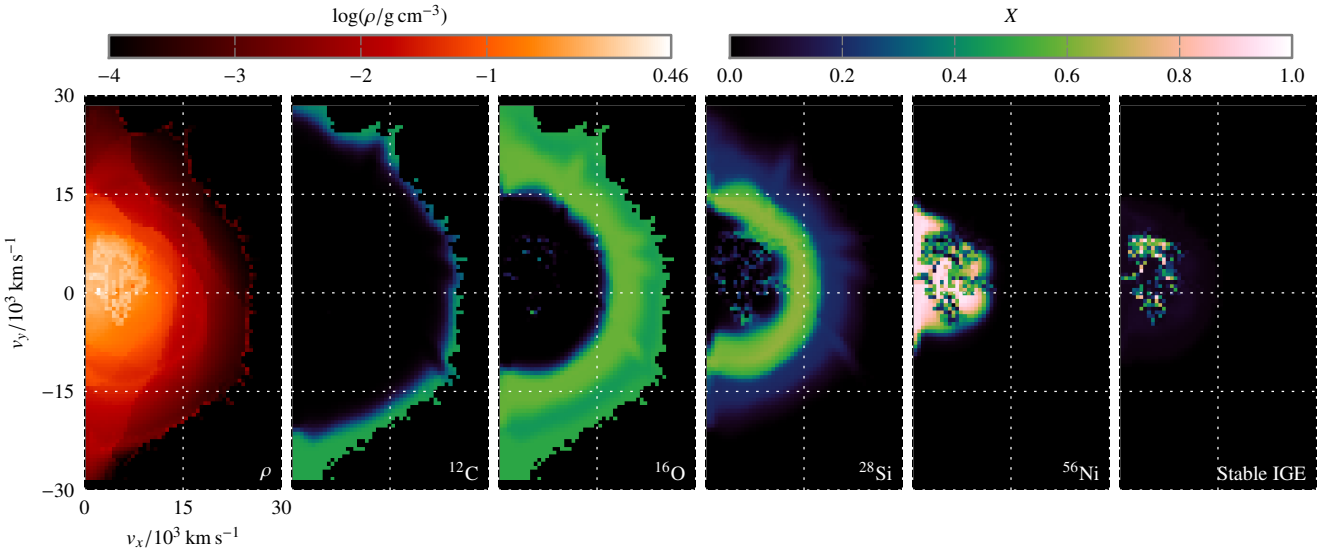

Fig. 5. Same as Fig. 4 for the 2D model rpc32_ddt2_dd080 producing 0.57 $M_\odot$ of ^{56}Ni.

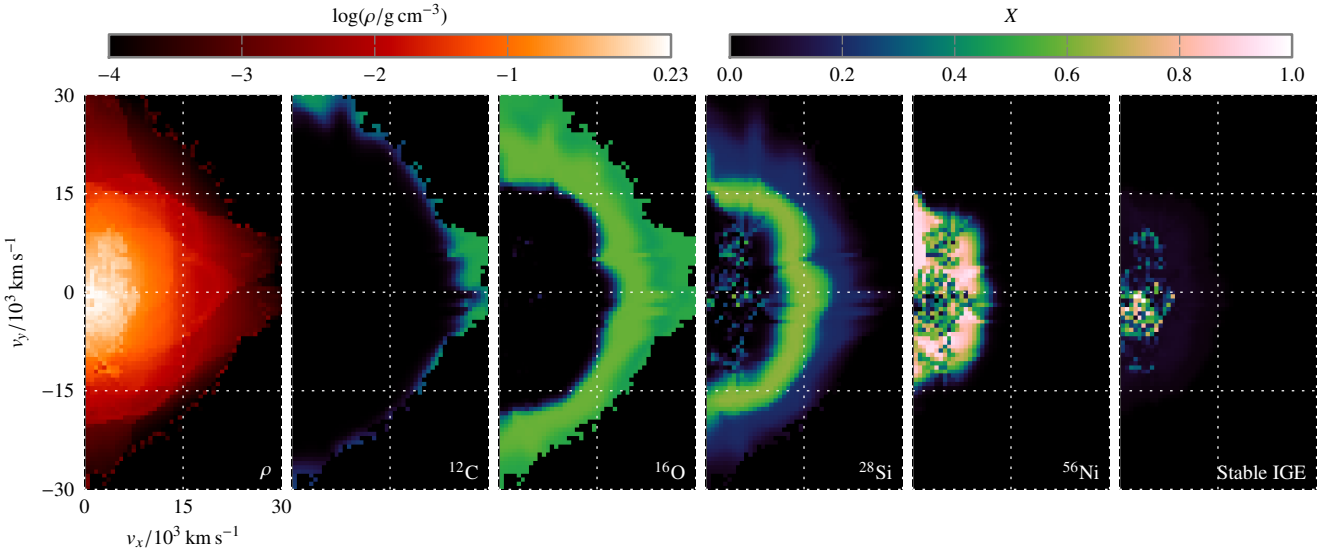

Fig. 6. Same as Fig. 4 for the 2D model c50_ddt2_dd150 producing 0.62 $M_\odot$ of ^{56}Ni.

Moreover, comparing the homogeneous models, the outer layers of the ejecta contain more unburnt material for a smaller C mass fraction (compared to the initial composition), which can be explained by less burning at these smaller densities for lower C mass fractions (see Appendix A). The more realistic model with a C depleted core resembles the 50% model in the outer layers (less unburnt material) and the 30% model in the inner layers (the ejecta are shifted to lower velocities).

4.2. 3D simulations

A few 3D full-star simulations with more realistic treatment of the 3D turbulent burning process have been conducted to quantify the impact of different compositions. In all simulations, the initial model is composed of a core of differing C mass fraction (0.2 to 0.5) which is surrounded by an outer layer with a C mass fraction of 0.5. General properties of the model and results from the radiative transfer simulations are presented in Table 2. The detailed nucleosynthetic abundances for selected models are given in Table 3 for radioactive isotopes after 100 s (this corresponds to the end of the simulation, when the expansion is nearly homologous) and in Table 4 for stable isotopes after 2 Gyr. For these models, the ^{56}Ni mass varies between 0.36 and 0.80 solar masses. The relative abundances (normalized to ^{56}Fe) compared to solar values do not show large changes for different composition; here, metallicity (i.e., mainly the neutron-rich isotope ^{22}Ne after He burning) plays a larger role (see Seitenzahl et al. 2013, Fig. 7).

When the different parameters (ignition conditions, DDT criteria, and initial compositions) are varied, the hydrodynamic evolution in the 3D models shows similarities to the 2D models. This can be seen for different initial compositions, e.g., in the evolution of the nuclear energy, which is shown in Fig. 7 for selected 3D models. The main difference between the evolution in 2D and 3D models is the slower energy release in 3D which is due to burning starting from spheres unlike tori in 2D-axisymmetric geometry. Hence, the deflagration transitions later to the turbulent regime driven by the Rayleigh-Taylor instability.

In Fig. 7, a dot indicates the time when the first DDT is initiated and thus marks the transition to the detonation phase. Model rpc20_DDT8_N100 fails to initiate a detonation because the released nuclear energy does not generate enough turbulent motions to trigger the DDT[1]. As this model is simply a pure deflagration (also called "failed detonation" by Jordan et al. 2012b; Fink et al. 2014, see there for recent models), it will not be discussed further. Nevertheless it is interesting that the DDT criterion chosen here fails for some models, while it successfully initiates a detonation for other models. For the model series with varying C fraction, the nuclear energy release during the deflagration phase rises with the carbon mass fraction as expected from the binding energy differences and from the calibration (see Appendix A). This leads to the DDT criterion being fulfilled earlier for larger C mass fractions; thus, the expansion of the WD is smaller and unburnt material is present at higher densities. The detonation consumes the remaining unburnt material; and for higher densities, more ^{56}Ni is produced. Moreover, for larger C mass fractions, the transition density to burning to NSE

[1] The DDT criterion chosen here requires high turbulent velocity fluctuations $\geq 10^8$ cm s^{-1} to be present with a certain probability for at least half an eddy-turnover-time; this is the same criterion as used by Seitenzahl et al. (2013). More details on the treatment of the criterion are described by Ciaraldi-Schoolmann et al. (2013).

Table 2. Average initial C mass fraction, ^{56}Ni mass, asymptotic kinetic energy, rise time to B-band maximum, peak magnitudes, decline rate, and spectral velocities of the Si II feature at λ6355 Å.

Model	$\overline{X}_0(^{12}\mathrm{C})$	$M(^{56}\mathrm{Ni})$ ($M_\odot$)	$E_{\mathrm{kin,a}}$ (10^{51} erg)	$t(B_{\max})$ (d)	$U_{\max}$ (mag)	$B_{\max}$ (mag)	$V_{\max}$ (mag)	$R_{\max}$ (mag)	$I_{\max}$ (mag)	$\Delta m_{15}(B)$ (mag)	$v_{\mathrm{Si}}(t_{B_{\max}})$ (10^3 km s^{-1})
rpc20_DDT8_N100	0.26	0.364	0.43	–	–	–	–	–	–	–	–
rpc32_DDT8_N100	0.36	0.603	1.28	17.4	−18.9	−19.0	−19.5	−19.5	−19.5	1.41	12.5
rpc40_DDT8_N100	0.42	0.701	1.43	17.5	−19.1	−19.2	−19.7	−19.6	−19.5	1.49	13.5
c50_DDT8_N100	0.50	0.799	1.54	17.3	−19.4	−19.4	−19.9	−19.7	−19.6	1.55	14.4
N100 (Seitenzahl et al. 2013)	0.50	0.604	1.44	16.6	−18.8	−19.0	−19.5	−19.6	−19.6	1.42	13.1

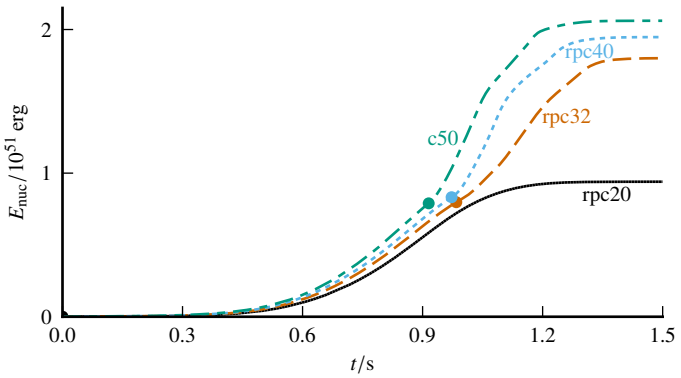

Fig. 7. Evolution of nuclear energy in time for several 3D simulations with different initial compositions but otherwise identical explosion parameters (models rpc20_DDT8_N100, rpc32_DDT8_N100, rpc40_DDT8_N100, c50_DDT8_N100; inner core of 20%, 32%, 40% and 50% C by mass, respectively). The dot marks the point of the first DDT. The rpc20 model failed to initiate a detonation for this DDT criterion.

is smaller, adding to the effect of producing more NSE material for larger C mass fractions and thereby releasing more nuclear energy. The ^{56}Ni mass follows a similar linear relation for the carbon mass fraction with a slope near 1, similar to the mean relation found for the 2D models (cf. Eq. (1) and values in Tables 2 and 3).

Apart from examining the influence of each parameter separately, several parameters can be changed at once to create models with similar ^{56}Ni yields. As these models will show similar peak luminosities (dominated by the total amount of ^{56}Ni), they can be compared in their ability to explain the same SN, as opposed to explaining SNe Ia in general. The spherically averaged ejecta distribution in velocity space is compared for two 3D models with similar ^{56}Ni masses of about 0.6 $M_\odot$ in Fig. 8: the first panel shows the homogeneous model (in initial composition) N100 from Seitenzahl et al. 2013, in the second panel the C depleted model rpc32_DDT8_N100 is plotted. The C depleted model features a lower asymptotic kinetic energy of 1.28×10^{51} erg compared to the homogeneous model (1.44×10^{51} erg). The global structure of the ejecta is similar to the 2D models (Figs. 4–6): outer layers of C, O and Si and a core consisting mainly of ^{56}Ni and stable IGE. The stable iron group elements are created mainly in the deflagration ashes during normal freeze-out from NSE. This is also the reason for the stable iron group elements extending to rather high velocities for both models, up to $\sim 15 \times 10^3$ km s^{-1}. They are created during the deflagration phase in the rising hot plumes, thus being present at large radii and velocities[2]. Despite the larger kinetic energy in the homogeneous model, the velocities in the ejecta tend to be only slightly larger than in the carbon depleted model with similar ^{56}Ni mass (see first and second panel of Fig. 8). Especially the outer boundary of the Ni core and the maximum of the Si distribution are shifted by only a few 100 km s^{-1}. Moreover, more unburnt material is present in the C depleted model mostly because of the shift in the burning tables (see Appendix A). When comparing a model series with varying core C mass fraction (second, third, and fourth panel of Fig. 8), these effects can be seen more clearly as the kinetic energy of the ejecta increases with increasing C mass fraction and increasing production of ^{56}Ni.

[2] This is a general feature of multi-dimensional DDT models; as opposed to 1D models, where the stable iron group elements are concentrated near the center (see Fig. 2 from Khokhlov 1991b).

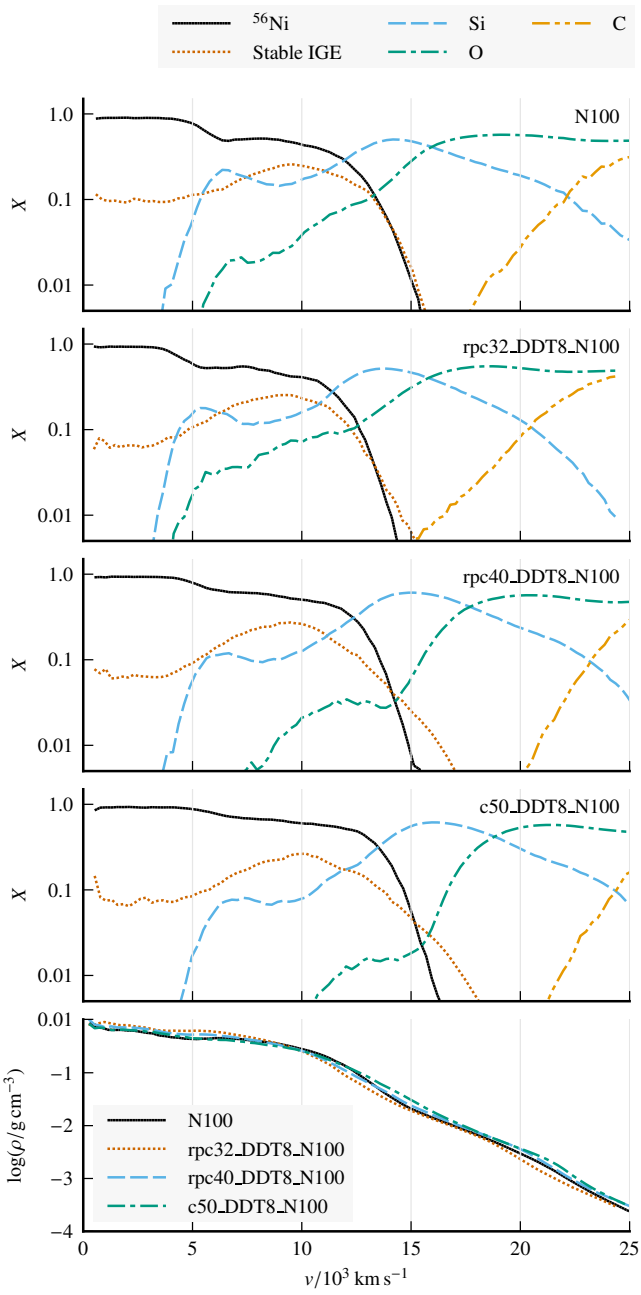

Fig. 8. Angle averaged ejecta distribution in velocity space for several 3D models 100 s after ignition. The model in the *top panel* is N100 from Seitenzahl et al. (2013). Shown are the mass fractions (*top panels*, stable IGE are all iron group elements with $Z > 20$ without ^{56}Ni) and the density (*bottom panel*).

The density structure (bottom panel of Fig. 8) is very similar for all models; thus, the differences in the spectra mainly stem from differences in the abundance distributions.

5. Synthetic observables

In this section, we present synthetic light curves and spectra from the radiative transfer simulations and compare to observed SNe. The effects of the initial composition are examined in two ways:

(i) by comparing a series of models with differing carbon mass fraction but otherwise identical explosion parameters, thus having different kinetic energies and ^{56}Ni masses;

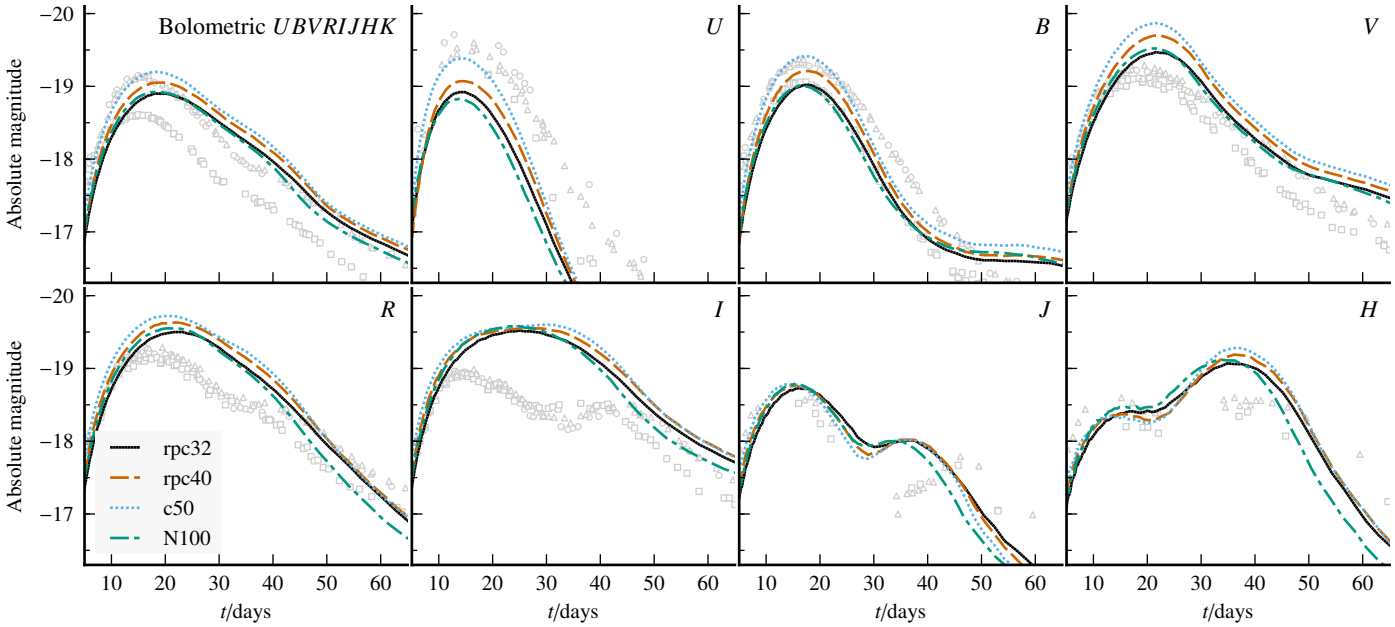

Fig. 9. Angle-averaged light curves for models rpc32_DDT8_N100, rpc40_DDT8_N100, c50_DDT8_N100, and N100 of Seitenzahl et al. (2013) (solid lines) compared to some normal SNe Ia (gray points; circles: SN 2003du, squares: SN 2004eo, triangles: SN 2005cf).

(ii) by comparing models with different carbon mass fraction producing a similar amount of ^{56}Ni while having different kinetic energies.

5.1. Light curves

Radiative transfer simulations were run for the DDT models compared in Fig. 7 (rpc32_DDT8_N100, rpc40_DDT8_N100, and c50_DDT8_N100). The ignition condition was chosen to be the same as for the N100 model of Seitenzahl et al. (2013) since the intermediate deflagration strength of this model leads to the best agreement with observed light curves and spectra in this series (Sim et al. 2013)[3]. Compared to the N100 model, the DDT criterion of the new models was adjusted such that the rpc32 model produces approximately 0.6 $M_\odot$ of ^{56}Ni, the same amount as the N100 model of Seitenzahl et al. (2013). Thus, these two models are very similar (apart from the initial composition) in order to assess the results of changing the initial C fraction.

The synthetic light curves from these models and the N100 model from Seitenzahl et al. (2013) are compared to some normal SNe Ia in Fig. 9. The peak luminosity of the bolometric and the band-limited light curves are larger for larger ^{56}Ni masses. The spread in peak luminosities is largest in the *U* band and decreases to redder bands, similar to what is found by Sim et al. (2013) for their model series.

The shapes of the light curves match observations quite well around maximum for *U*, *B*, and *V* bands, although the flux is too low in the *U* band and too high in the *V* band. Thus, the colors are too red compared to observed light curves (similar to the models of Sim et al. 2013). As already stated in Sim et al. (2013), this is probably due to line-blocking mainly of IGE in the blue part of the spectrum. This is a generic feature of their spontaneous DDT models caused by the deflagration ashes (which contain stable IGE) rising to rather high velocities, near the IME (as described above, see Fig. 8), hence influencing the synthetic observables in the photospheric phase. In contrast to this, in 1D models (see Fig. 2 from Khokhlov 1991b) the IGE are contained in the core of the ejecta beneath the radioactive ^{56}Ni owing to the spherical symmetry adopted in these models, neglecting the turbulent deflagration burning. Apart from this, the reddening could also be due to shortcomings in the radiative transfer treatment, as reproducing the colors in radiative transfer simulations of SNe Ia is in general difficult (Dessart et al. 2014b).

In the *I* band, the models deviate from observed light curves: they are too bright and do not show two maxima, similar to the models in Sim et al. (2013). Although this may be due to an incomplete treatment in the radiative transfer code affecting the Ca II infrared triplet, which significantly contributes to this band (Sim et al. 2013), this may also hint to the spontaneous DDT models being in general inferior to other models in this respect. For example, sub-Chandrasekhar models (Sim et al. 2010) or violent merger models (Pakmor et al. 2012b) show better agreement using the same radiative transfer code ARTIS (see also Sim et al. 2013).

In the near-infrared bands *J* and *H*, the models agree qualitatively with observations, matching the magnitudes at the first maximum and exhibiting a second maximum. The variations in these near-infrared bands are, especially at maximum, smaller than in the optical bands, which is also seen in observations showing that SNe Ia are better standard candles in the near-infrared (Elias et al. 1985; Meikle 2000; Krisciunas et al. 2004). Moreover, in these bands, the first maxima are larger compared to the light curves in Sim et al. (2013), thus agreeing better with observed light curves. As already predicted in Sim et al. (2013), this results from using a larger atomic data set, thus producing more fluorescence in the near-infrared. The position of the second maximum, however, is too early compared to observed light curves. The second maximum is caused by the recombination front from doubly to singly ionized material hitting the iron-rich core (Kasen 2006). Thus, the offset between simulations and observations could indicate that IGE reside at too large velocities

[3] This model was also compared to SN 2011fe alongside a double-degenerate violent merger model in Röpke et al. (2012).

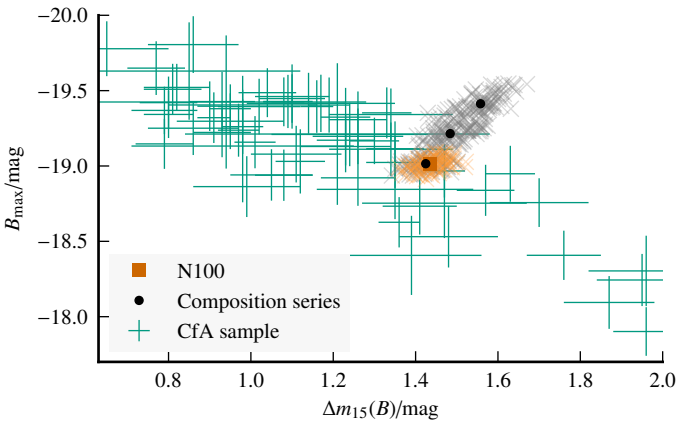

Fig. 10. Light curve width-luminosity relation for a series of models with differing C depletion in the core, but otherwise identical parameters (in black: models rpc32_DDT8_N100, rpc40_DDT8_N100, and c50_DDT8_N100 with increasing B_{max} in this order) as well as for the N100 model of Seitenzahl et al. (2013, in gold). The dots and the square denote angle-averaged values, pale crosses denote values for different lines of sight. The green crosses show observed supernovae from the CfA sample (Hicken et al. 2009).

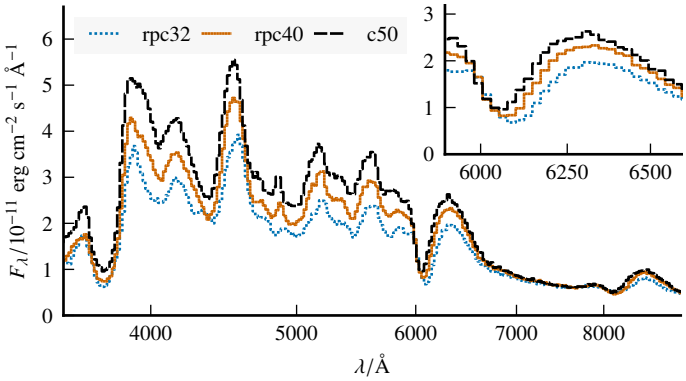

Fig. 11. Comparison of spectra around B-band maximum at 17.3 days post explosion for models rpc32_DDT8_N100, rpc40_DDT8_N100, and c50_DDT8_N100. The inset shows the Si II feature at λ6355 Å in more detail, the units are the same as in the main plot. All fluxes are scaled to a distance of 1 Mpc.

in our models. However, it could also be related to deficiencies in the numerical treatment, such as inaccurate atomic data or approximations in calculating the plasma state in ARTIS.

A comparison of the two models with similar ^{56}Ni masses (N100 from Seitenzahl et al. 2013 and rpc32_DDT8_N100) shows only slight differences. The main consequence on the light curve here is given by the different kinetic energies of the ejecta. According to the analytic study of bolometric light curve models by Pinto & Eastman (2000), models with larger kinetic energy "peak earlier, at higher luminosities, and decline more rapidly" (Pinto & Eastman 2000, see also their Fig. 4). This is indeed also found for the bolometric light curves of the models N100 from Seitenzahl et al. (2013) and rpc32_DDT8_N100 (see Fig. 9): the C depleted model peaks later and at a lower luminosity. Moreover, its decline rate is smaller. The effect is not as large as for the models in Pinto & Eastman (2000) because the total kinetic energy of the rpc32_DDT8_N100 model differs only by about 11% from the N100 model of Seitenzahl et al. (2013).

5.2. Width-luminosity relation

The decline in the B band of the models is more rapid than for most normal SNe Ia (Fig. 10). More importantly, the model series as a whole fails to show the same width-luminosity relation (WLR) as normal SNe Ia; in contrast, the WLR is roughly perpendicular to that observed (Fig. 10). The fundamental parameters for the light curve evolution that are changed in this model series are the kinetic energy of the ejecta and the ^{56}Ni mass, which both increase with increasing C fraction. According to the analytic study of light curves by Pinto & Eastman (2000), both of these parameters anti-correlate individually with the observed WLR. Therefore, it is not surprising to find an anti-correlation for our model series, where the increase in C fraction (as a physical parameter of the explosion model) leads to an increase in kinetic energy and ^{56}Ni mass, both driving a trend perpendicular to the observed WLR. This implies that the initial composition is probably not the main parameter driving the WLR, but rather a secondary parameter causing scatter perpendicular to the WLR. This is similar to orientation effects also driving scatter around the mean WLR.

The only possibility of driving the WLR in the direction that is observed would, in this model, be the existence of a correlation of the physical model parameters. In this case, the ignition configuration and the DDT criterion would depend on the initial composition (in a yet unknown way), thereby supposedly resulting in a suitable WLR. The 1D delayed detonation models of Höflich & Khokhlov (1996) show a WLR, where the changing parameter is the DDT transition density, but as this parametrization does not include turbulence, for example, it cannot be easily generalized to our multi-dimensional models. The 2D models of Kasen et al. (2009) lie in a reasonable region of the light curve width-luminosity diagram; this was reached by varying the ignition conditions for the deflagration as well as the DDT criterion. This model series faces the problem that the correlation between the varying explosion parameters and the underlying physical parameters of the initial model (such as central density, composition or metallicity) is not known and thus does not identify the physical parameter driving the WLR.

5.3. Spectra

The synthetic spectra of the model series are shown in Fig. 11 at B-band maximum. They share all main spectral features and differ mostly in the absolute flux values (Fig. 11). Moreover, the Si II feature at λ6355 Å varies in blue shift for different models: with increasing C mass fraction, the absorption feature shifts from 12.5 × 10^3 km s^{-1} (rpc32) to 14.4 × 10^3 km s^{-1} (c50), thus reflecting the change in the velocity distributions (compare Fig. 8). The features associated with Ca II[4], however, are not shifted in wavelength for different models.

A comparison between two models with similar ^{56}Ni mass but different kinetic energies (rpc32_DDT8_N100 and N100 from Seitenzahl et al. 2013, see Fig. 12) shows that the C depleted model shifts in velocities only by about 600 km s^{-1} at B-band maximum because of the lower kinetic energy of the ejecta. Comparing to observations, this shift goes in the right direction but is not large enough to account for the lower velocities in, e.g., SN 2011fe, as shown for several epochs in Fig. 12. Moreover, the bulk of observed SNe shows considerably lower velocities, mostly between 10 000 km s^{-1} and 12 000 km s^{-1} at B-band maximum (Benetti et al. 2005; Silverman et al. 2012).

[4] The Ca II H & K lines ($\lambda\lambda$3934 and 3968 Å) and the Ca II infrared triplet.

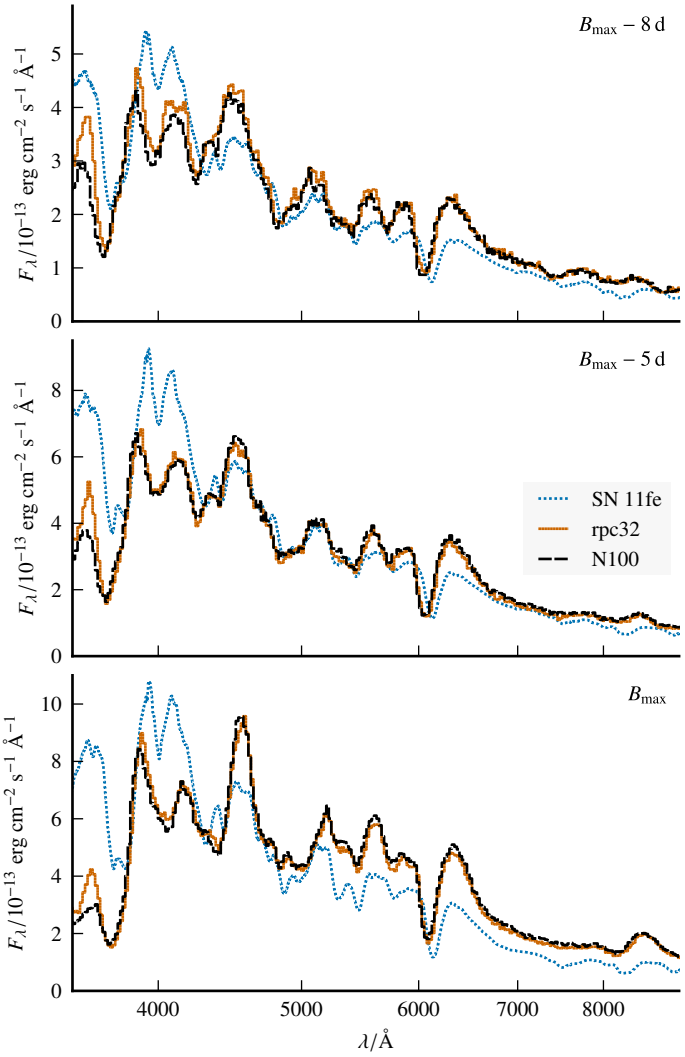

Fig. 12. Comparison of spectra for three epochs (8 d before, 5 d before and at *B*-band maximum) of models rpc32_DDT8_N100, and N100 of Seitenzahl et al. (2013) to SN 2011fe. The flux is scaled to M101, the host galaxy of SN 2011fe.

The magnitude of this effect can be estimated by assuming that the velocities in the two models scale with the square root of the kinetic energy, $\frac{\bar{v}_1}{\bar{v}_2} = \sqrt{\frac{E_{\rm kin,1}}{E_{\rm kin,2}}}$. A change in the kinetic energies from N100 to the rpc32 model of about 11% hence results in a change in velocities of about 6%, which yields about 750 km s^{-1} for the Si II velocity, on the order of the change seen in the models.

This seems to be a shortcoming of the spontaneous DDT model, also present in our previous model series (Seitenzahl et al. 2013; Sim et al. 2013), but also in studies of other groups (e.g., the DDC models from Dessart et al. 2014a, see their Fig. 17; these models are based on explosion simulations of Khokhlov 1991a).

Thus, if explosions from Chandrasekhar-mass WDs constitute a large fraction of normal SNe Ia, the nucleosynthetic yields (and thus the energy release) could be affected by uncertainties in the nuclear reaction rates. Alternatively, the mechanism that distorts the hydrostatic equilibrium of the WD[5] may not involve a direct transition from the deflagration to a detonation, as in our spontaneous DDT models, but perhaps other large-scale motions (e.g., pulsations).

[5] This is needed for the detonation to propagate through lower-density, pre-expanded material such that also IME are produced.

5.4. Comparison to earlier studies

Höflich et al. (1998) presented a series of 1D delayed detonation models (including hydrodynamics, nucleosynthesis, light curves, and spectra) with varying metallicity and included one model with a different C fraction. Their 1D models treat the deflagration as propagating at a certain fraction of the local sound speed; the transition to a detonation is initiated when a certain density is reached. Despite these simplifications, their conclusions are similar to our findings: a lower C fraction leads to lower ^{56}Ni production, less kinetic energy, and more confined ejecta. Their C reduced model shows a faster decline, as opposed to what is seen in our models and expected for lower kinetic energies according to the analytic study of Pinto & Eastman (2000). They also mention that more realistic structures of the progenitor composition should be taken into account including an outer accretion layer and a C depleted core; this was accomplished in the present study. Their assumption, however, that a model with a homogeneous, but lower C fraction does not show a difference to a model with a C depleted core (see their "Final Discussion and Conclusions") holds only to a first approximation. As the propagation of the burning fronts does not only depend on density, but also on the composition (see Appendix A), the energy release and burning products of the detonation in the outer layers depend on the composition there.

The 1D simulations by Umeda et al. (1999a) include only hydrodynamics and nucleosynthesis of delayed detonation models, where the DDT density depends on the initial C fraction. In contrast to this, our DDT criterion includes different effects as, e.g., turbulent velocity fluctuations (see Sect. 3.2). Nevertheless, this leads to a similar result: the density at which the detonation is initiated decreases for decreasing C fractions. Thus, in their model series, the produced amount of ^{56}Ni decreases for decreasing C fractions (see their Fig. 2). Apart from this, the working hypothesis of Umeda et al. (1999a), who assume the C mass fraction to be responsible for the WLR, is challenged by our findings.

In their study of 1D delayed detonation models, Domínguez et al. (2001) compute stellar models for different ZAMS masses and metallicities which they use as initial models for the explosion simulations. All models use the same central density at explosion and employ the same density as DDT criterion, but do not take the pre-explosion simmering phase into account. They find that for larger ZAMS masses, less ^{56}Ni is produced because of the lower C abundance, resulting in lower velocities in the ejecta, similar to our findings. This leads in their models to a decrease in the maximum brightness, while the decline rate stays constant. Thus, Domínguez et al. (2001) conclude that the variation in the ZAMS mass leads to a spread or offset in the WLR, similar to what we find for the initial C mass fraction.

Höflich et al. (2010) suggest that in addition to the primary light curve parameter, Δm_{15} or stretch s, two independent parameters are necessary to describe the differences in shapes for different SNe. As physical parameters they suggest C/O ratio and central density to account for different shapes in the early and late phase of the light curve, respectively. In the 1D models of Höflich et al. (2010), the transition density of the DDT determines the ^{56}Ni mass of the explosion; the impact of other parameters (C/O ratio, central density) on the intrinsic brightness is small; nevertheless, these variations should be taken into account in the calibration. Our study agrees on the C fraction

being a secondary parameter in the family of SN Ia light curves. In our 3D models, however, the C fraction causes large variations in the ^{56}Ni mass because of the different turbulent evolution of the deflagration flame and the resulting different triggering of the DDT. This should be taken into account when trying to create a physically motivated multi-parameter set for SN Ia light curves.

The first multi-dimensional simulations examining different C fractions were presented by Röpke & Hillebrandt (2004) and Röpke et al. (2006a). In their 3D simulations of pure deflagrations, the C fraction does not affect the explosion significantly; only the kinetic energy of the ejecta is altered to some extent. Therefore, they conclude that "the progenitor's carbon-to-oxygen ratio is unlikely to account for the observed variations in type Ia supernova luminosity" (Röpke & Hillebrandt 2004). This statement only holds for pure deflagration models, which nowadays are thought to account rather for 2002cx-like SNe Ia than for normal SNe Ia (Jordan et al. 2012a; Kromer et al. 2013; Fink et al. 2014) because of their mixed ejecta structure in contrast to the layered structure seen in normal SNe Ia. Thus, their statement does not apply to modeling normal SNe Ia and it does not contradict our results for delayed detonation models.

6. Conclusions

In this work, we study the hydrodynamics, nucleosynthesis, synthetic light curves, and synthetic spectra of a series of multi-dimensional spontaneous DDT models for SNe Ia in order to examine if varying the initial C fraction resolves remaining discrepancies to observations. The main points we consider are the WLR resulting from the models and differences in spectral features.

Firstly, the initial C mass fraction is not the primary parameter of SNe Ia (at least for spontaneous DDT models). Although absolute luminosities ($B_{\max}$ between -19.0 and -19.4) and decline rates ($\Delta m_{15}(B)$ between 1.41 and 1.55) are in the range of normal SNe Ia, respectively, our model series fails to reproduce the observed WLR (Fig. 10). Therefore, it is probably only a secondary parameter causing scatter perpendicular to the observed WLR. This may only be changed by a concerted correlation of the different physical parameters of the underlying explosion model, such as ignition conditions or DDT criteria.

Secondly, carbon depleted models do not show significantly better agreement of important spectral features, such as the Si II feature at λ6355 Å. The decrease in kinetic energy does not lead to a decrease in the blueshift of the feature to be compatible with the bulk of normal SNe Ia. This shortcoming seems to be generally present in spontaneous DDT models (1D, 3D, different groups; see discussion above).

Finally, our spontaneous DDT models are able to reproduce most of the observed properties of SNe Ia light curves and spectra, thus supporting the spontaneous DDT model. So far, however, our 3D spontaneous DDT models do not show the observed width-luminosity relation. While the deflagration strength (through number of ignition kernels, Seitenzahl et al. 2013; Sim et al. 2013) and the initial C fraction (this work) are not the primary parameter, it may still be possible that other parameters (e.g., DDT criterion) or yet unknown correlations of parameters are able to reproduce the light curve width-luminosity relation in 3D models. Nevertheless, other shortcomings remain, such as colors, which are too red (Sim et al. 2013), and the velocities of spectral features, especially the Si II feature that is defining SNe Ia. This may be interpreted in different ways: if Chandrasekhar-mass progenitors are indeed responsible for the bulk of SNe Ia, the spontaneous DDT model has some severe shortcomings; this may hint to the possibility that a different mechanism distorts the hydrostatic equilibrium of the WD and leads to a detonation (e.g., pulsations). Apart from this, the failure of recent multi-dimensional DDT models to identify the primary parameter of the WLR could also indicate that this primary parameter is the mass of the primary WD[6], as is the case in detonations of sub-Chandrasekhar-mass WDs either in a double degenerate binary (violent merger scenario, e.g., Pakmor et al. 2012b, 2013) or in a single degenerate system (double detonation scenario, e.g., Fink et al. 2010).

Acknowledgements. The 3D models have been computed on the supercomputers JUGENE and JUQUEEN at the Jülich Supercomputer Center under the project HMU13. This work was also supported by the Deutsche Forschungsgemeinschaft via the Transregional Collaborative Research Center TRR 33 "The Dark Universe", the Emmy Noether Program (RO 3676/1-1), the ARCHES prize of the German Ministry of Education and Research (BMBF), the graduate school "Theoretical Astrophysics and Particle Physics" at the University of Würzburg (GRK 1147) and the Excellence Cluster EXC 153. Parts of this research were conducted by the Australian Research Council Centre of Excellence for All-sky Astrophysics (CAASTRO), through project number CE110001020. S.T.O. acknowledges support from the Studienstiftung des deutschen Volkes and thanks S. Hachinger for valuable dicussions. R.P. acknowledges support by the European Research Council under ERC-StG grant EXAGAL-308037 and by the Klaus Tschira Foundation. M.F., S.A.S., and F.K.R. acknowledge travel support by the DAAD/Go8 German-Australian exchange program. We thank S. Taubenberger for providing the data of the CfA sample. For data processing and plotting, we used NumPy and SciPy (Oliphant 2007), IPython (Pérez & Granger 2007), and Matplotlib (Hunter 2007).

Appendix A: Iterative calibration of the levelset tables

The tables necessary for determining the composition behind the burning fronts are created using an iterative calibration scheme similar to Fink et al. (2010). This calibration scheme is carried out for homogeneous compositions of the progenitor WD ($X(^{12}\mathrm{C}) = 0.2, 0.3, \ldots, 0.9$), separately for deflagrations and detonations. It yields the composition behind the burning front as a function of the density of the unburnt material.

Each calibration run uses as an initial estimate burning to NSE at the relevant densities (detonations: above 10^5 g cm^{-3}; deflagrations: above 2×10^5 g cm^{-3}), such that the energy release is overestimated. The table with the nucleosynthetic yields of this initial estimate as a function of density is used in a hydrodynamic simulation of a pure detonation or deflagration, followed by a nucleosynthetic postprocessing. A new table is then computed with the detailed nucleosynthetic yields for use in the next hydrodynamic simulation. This procedure is iterated six times for each calibration run. As an example, the final table for $X(^{12}\mathrm{C}) = 0.5$ for detonations is shown in Fig. A.1. The transitions to different burning stages (C burning, O burning, Si burning) are clearly visible. The convergence of this scheme is based on the fact that the reaction rates depend strongly on density. The overestimation of the energy release in the first hydrodynamic simulation is thus decreased by the subsequent postprocessing, since the density of unburnt material prior to the front crossing is not strongly affected by a larger energy release.

The influence of the initial composition on the final tables is better seen by comparing the reaction Q value, which is the energy release of the burning front. The Q value is shown for different initial compositions in the upper panel of Fig. A.2 for detonations and in the lower panel of Fig. A.2 for deflagrations.

[6] This was already suspected by Pinto & Eastman (2000) in their analytic study of light curves and is supported by observations of Stritzinger et al. (2006) and Scalzo et al. (2014).

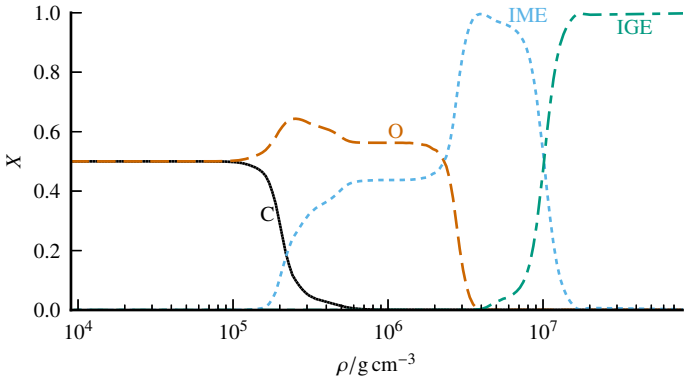

Fig. A.1. Levelset table for a detonation with an initial composition of $X(^{12}\mathrm{C}) = 0.5$. We show the mass fractions of C, O, intermediate mass elements (IME) and iron group elements (IGE), which are released behind the front, against the density of the unburnt material.

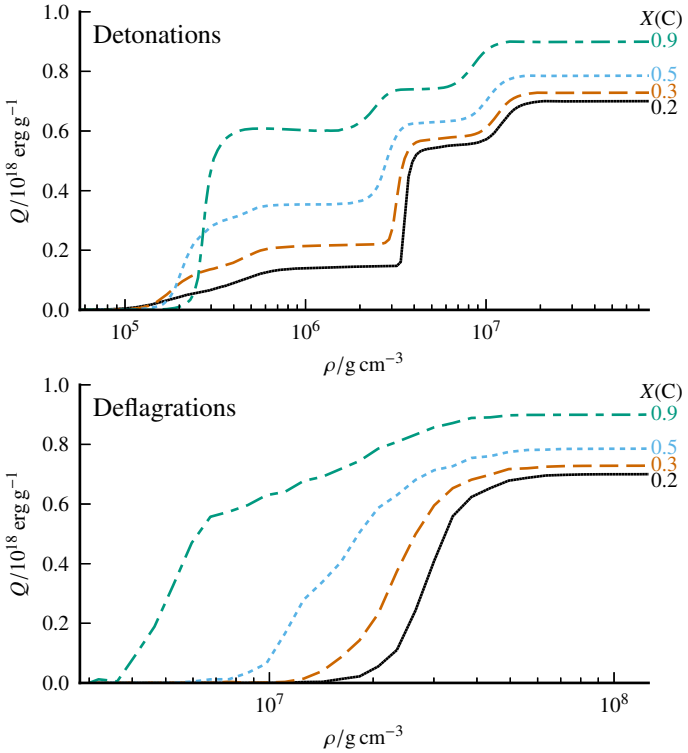

Fig. A.2. Q value (energy release behind burning front) of levelset tables for selected initial compositions for detonations (*upper panel*) and deflagrations (*lower panel*).

The tables differ mainly in the density interval over which the composition changes; it is wider and extends to lower densities for detonations. Apart from this, the shape is different, as in the tables for deflagrations the transitions to the different burning stages are not separated. For both detonations and deflagrations, the Q value is globally lower for lower carbon mass fractions. Moreover, the transitions to the different burning stages shift to higher densities for lower carbon mass fractions. Globally seen, this leads to a *weaker development* of both detonations and deflagrations for lower carbon mass fractions.

References

Arnett, W. D., Truran, J. W., & Woosley, S. E. 1971, ApJ, 165, 87
Asplund, M., Grevesse, N., Sauval, A. J., & Scott, P. 2009, ARA&A, 47, 481
Benetti, S., Cappellaro, E., Mazzali, P. A., et al. 2005, ApJ, 623, 1011
Blinnikov, S. I., & Khokhlov, A. M. 1986, Sov. Astron. Lett., 12, 131
Branch, D., Fisher, A., & Nugent, P. 1993, AJ, 106, 2383
Bravo, E., & García-Senz, D. 2008, A&A, 478, 843
Bravo, E., & García-Senz, D. 2009, ApJ, 695, 1244
Bravo, E., García-Senz, D., Cabezón, R. M., & Domínguez, I. 2009, ApJ, 695, 1257
Bravo, E., Piersanti, L., Domínguez, I., et al. 2011, A&A, 535, A114
Chandrasekhar, S. 1931, ApJ, 74, 81
Ciaraldi-Schoolmann, F., Seitenzahl, I. R., & Röpke, F. K. 2013, A&A, 559, A117
Colella, P., & Glaz, H. M. 1985, J. Comput. Phys., 59, 264
Colella, P., & Woodward, P. R. 1984, J. Comput. Phys., 54, 174
Dessart, L., Blondin, S., Hillier, D. J., & Khokhlov, A. 2014a, MNRAS, 441, 532
Dessart, L., Hillier, D. J., Blondin, S., & Khokhlov, A. 2014b, MNRAS, 441, 3249
Domínguez, I., Höflich, P., & Straniero, O. 2001, ApJ, 557, 279
Elias, J. H., Matthews, K., Neugebauer, G., & Persson, S. E. 1985, ApJ, 296, 379
Fink, M., Hillebrandt, W., & Röpke, F. K. 2007, A&A, 476, 1133
Fink, M., Röpke, F. K., Hillebrandt, W., et al. 2010, A&A, 514, A53
Fink, M., Kromer, M., Seitenzahl, I. R., et al. 2014, MNRAS, 438, 1762
Fryxell, B. A., Müller, E., & Arnett, W. D. 1989, Hydrodynamics and nuclear burning, MPA Green Report 449, Max-Planck-Institut für Astrophysik, Garching
Gall, E. E. E., Taubenberger, S., Kromer, M., et al. 2012, MNRAS, 427, 994
Gamezo, V. N., Khokhlov, A. M., & Oran, E. S. 2005, ApJ, 623, 337
García-Senz, D., Cabezón, R. M., Arcones, A., Relaño, A., & Thielemann, F. K. 2013, MNRAS, 436, 3413
Golombek, I., & Niemeyer, J. C. 2005, A&A, 438, 611
Hicken, M., Challis, P., Jha, S., et al. 2009, ApJ, 700, 331
Hillebrandt, W., & Niemeyer, J. C. 2000, ARA&A, 38, 191
Hillebrandt, W., Kromer, M., Röpke, F. K., & Ruiter, A. J. 2013, Frontiers of Physics, 8, 116
Höflich, P., & Khokhlov, A. 1996, ApJ, 457, 500
Höflich, P., & Stein, J. 2002, ApJ, 568, 779
Höflich, P., Wheeler, J. C., & Thielemann, F. K. 1998, ApJ, 495, 617
Höflich, P., Krisciunas, K., Khokhlov, A. M., et al. 2010, ApJ, 710, 444
Hunter, J. D. 2007, Comput. Sci. Eng., 9, 90
Iwamoto, K., Brachwitz, F., Nomoto, K., et al. 1999, ApJS, 125, 439
Jackson, A. P., Calder, A. C., Townsley, D. M., et al. 2010, ApJ, 720, 99
Jordan, IV, G. C., Fisher, R. T., Townsley, D. M., et al. 2008, ApJ, 681, 1448
Jordan, IV, G. C., Graziani, C., Fisher, R. T., et al. 2012a, ApJ, 759, 53
Jordan, IV, G. C., Perets, H. B., Fisher, R. T., & van Rossum, D. R. 2012b, ApJ, 761, L23
Kasen, D. 2006, ApJ, 649, 939
Kasen, D., Röpke, F. K., & Woosley, S. E. 2009, Nature, 460, 869
Khokhlov, A. M. 1991a, A&A, 245, 114
Khokhlov, A. M. 1991b, A&A, 245, L25
Krisciunas, K., Phillips, M. M., & Suntzeff, N. B. 2004, ApJ, 602, L81
Kromer, M., & Sim, S. A. 2009, MNRAS, 398, 1809
Kromer, M., Sim, S. A., Fink, M., et al. 2010, ApJ, 719, 1067
Kromer, M., Fink, M., Stanishev, V., et al. 2013, MNRAS, 429, 2287
Krueger, B. K., Jackson, A. P., Townsley, D. M., et al. 2010, ApJ, 719, L5
Kuhlen, M., Woosley, S. E., & Glatzmaier, G. A. 2006, ApJ, 640, 407
Kushnir, D., Katz, B., Dong, S., Livne, E., & Fernández, R. 2013, ApJ, 778, L37
Leibundgut, B. 2008, General Relativity and Gravitation, 40, 221
Lesaffre, P., Podsiadlowski, P., & Tout, C. A. 2005, MNRAS, 356, 131
Lesaffre, P., Han, Z., Tout, C. A., Podsiadlowski, P., & Martin, R. G. 2006, MNRAS, 368, 187
Li, W., Bloom, J. S., Podsiadlowski, P., et al. 2011, Nature, 480, 348
Lisewski, A. M., Hillebrandt, W., & Woosley, S. E. 2000, ApJ, 538, 831
Ma, H., Woosley, S. E., Malone, C. M., Almgren, A., & Bell, J. 2013, ApJ, 771, 58
Mazzali, P. A., Röpke, F. K., Benetti, S., & Hillebrandt, W. 2007, Science, 315, 825
Meikle, W. P. S. 2000, MNRAS, 314, 782
Moll, R., & Woosley, S. E. 2013, ApJ, 774, 137
Moll, R., Raskin, C., Kasen, D., & Woosley, S. 2014, ApJ, 785, 105
Nagataki, S., Hashimoto, M., Sato, K., & Yamada, S. 1997, ApJ, 486, 1026
Niemeyer, J. C., & Hillebrandt, W. 1995, ApJ, 452, 769
Niemeyer, J. C., & Woosley, S. E. 1997, ApJ, 475, 740
Oliphant, T. E. 2007, Comput. Sci. Eng., 9, 10
Osher, S., & Sethian, J. A. 1988, J. Comput. Phys., 79, 12
Pakmor, R., Edelmann, P., Röpke, F. K., & Hillebrandt, W. 2012a, MNRAS, 424, 2222
Pakmor, R., Kromer, M., Taubenberger, S., et al. 2012b, ApJ, 747, L10
Pakmor, R., Kromer, M., Taubenberger, S., & Springel, V. 2013, ApJ, 770, L8
Pérez, F., & Granger, B. E. 2007, Comput. Sci. Eng., 9, 21

Perlmutter, S., Aldering, G., Goldhaber, G., et al. 1999, ApJ, 517, 565
Phillips, M. M. 1993, ApJ, 413, L105
Pinto, P. A., & Eastman, R. G. 2000, ApJ, 530, 744
Piro, A. L., & Chang, P. 2008, ApJ, 678, 1158
Pskovskii, I. P. 1977, Sov. Astron., 21, 675
Raskin, C., Timmes, F. X., Scannapieco, E., Diehl, S., & Fryer, C. 2009, MNRAS, 399, L156
Raskin, C., Kasen, D., Moll, R., Schwab, J., & Woosley, S. 2014, ApJ, 788, 75
Reinecke, M., Hillebrandt, W., Niemeyer, J. C., Klein, R., & Gröbl, A. 1999, A&A, 347, 724
Reinecke, M., Hillebrandt, W., & Niemeyer, J. C. 2002, A&A, 386, 936
Riess, A. G., Filippenko, A. V., Challis, P., et al. 1998, AJ, 116, 1009
Roelofs, G., Bassa, C., Voss, R., & Nelemans, G. 2008, MNRAS, 391, 290
Röpke, F. K. 2007, ApJ, 668, 1103
Röpke, F. K. 2008, Proceedings of Science [arXiv:0804.2147]
Röpke, F. K., & Hillebrandt, W. 2004, A&A, 420, L1
Röpke, F. K., & Niemeyer, J. C. 2007, A&A, 464, 683
Röpke, F. K., Gieseler, M., Reinecke, M., Travaglio, C., & Hillebrandt, W. 2006a, A&A, 453, 203
Röpke, F. K., Hillebrandt, W., Niemeyer, J. C., & Woosley, S. E. 2006b, A&A, 448, 1
Röpke, F. K., Kromer, M., Seitenzahl, I. R., et al. 2012, ApJ, 750, L19
Rosswog, S., Kasen, D., Guillochon, J., & Ramirez-Ruiz, E. 2009, ApJ, 705, L128
Scalzo, R., Aldering, G., Antilogus, P., et al. 2014, MNRAS, 440, 1498
Schmidt, B. P., Suntzeff, N. B., Phillips, M. M., et al. 1998, ApJ, 507, 46
Schmidt, W., Niemeyer, J. C., & Hillebrandt, W. 2006a, A&A, 450, 265
Schmidt, W., Niemeyer, J. C., Hillebrandt, W., & Röpke, F. K. 2006b, A&A, 450, 283
Seitenzahl, I. R., Röpke, F. K., Fink, M., & Pakmor, R. 2010, MNRAS, 407, 2297
Seitenzahl, I. R., Ciaraldi-Schoolmann, F., & Röpke, F. K. 2011, MNRAS, 414, 2709
Seitenzahl, I. R., Ciaraldi-Schoolmann, F., Röpke, F. K., et al. 2013, MNRAS, 429, 1156
Silverman, J. M., Kong, J. J., & Filippenko, A. V. 2012, MNRAS, 425, 1819
Sim, S. A. 2007, MNRAS, 375, 154
Sim, S. A., Röpke, F. K., Hillebrandt, W., et al. 2010, ApJ, 714, L52
Sim, S. A., Seitenzahl, I. R., Kromer, M., et al. 2013, MNRAS, 436, 333
Soker, N., García-Berro, E., & Althaus, L. G. 2014, MNRAS, 437, L66
Stritzinger, M., Leibundgut, B., Walch, S., & Contardo, G. 2006, A&A, 450, 241
Thielemann, F.-K., Nomoto, K., & Yokoi, K. 1986, A&A, 158, 17
Thielemann, F.-K., Nomoto, K., & Hashimoto, M.-A. 1996, ApJ, 460, 408
Timmes, F. X., & Swesty, F. D. 2000, ApJS, 126, 501
Timmes, F. X., Brown, E. F., & Truran, J. W. 2003, ApJ, 590, L83
Townsley, D. M., Jackson, A. P., Calder, A. C., et al. 2009, ApJ, 701, 1582
Travaglio, C., Hillebrandt, W., Reinecke, M., & Thielemann, F.-K. 2004, A&A, 425, 1029
Travaglio, C., Hillebrandt, W., & Reinecke, M. 2005, A&A, 443, 1007
Umeda, H., Nomoto, K., Kobayashi, C., Hachisu, I., & Kato, M. 1999a, ApJ, 522, L43
Umeda, H., Nomoto, K., Yamaoka, H., & Wanajo, S. 1999b, ApJ, 513, 861
Woosley, S. E. 2007, ApJ, 668, 1109
Woosley, S. E., Kerstein, A. R., Sankaran, V., Aspden, A. J., & Röpke, F. K. 2009, ApJ, 704, 255
Zel'dovich, Y. B., Librovich, V. B., Makhviladze, G. M., & Sivashinskii, G. I. 1970, J. Appl. Mech. Techn. Phys., 11, 264
Zingale, M., Almgren, A. S., Bell, J. B., Nonaka, A., & Woosley, S. E. 2009, ApJ, 704, 196

Page 16 is available in the electronic edition of the journal at http://www.aanda.org

Table 3. Nucleosynthetic yields of radioactive isotopes (in solar masses) after 100 s for different DDT8_N100 models.

	rpc32	rpc40	c50
^{14}C	1.57E−06	3.62E−07	2.41E−07
^{22}Na	9.06E−09	2.01E−09	1.18E−09
^{26}Al	7.45E−07	2.02E−07	1.26E−07
^{32}Si	5.34E−09	1.34E−09	8.79E−10
^{32}P	2.22E−07	1.05E−07	7.02E−08
^{33}P	1.73E−07	8.07E−08	5.22E−08
^{35}S	1.78E−07	6.11E−08	3.83E−08
^{36}Cl	3.50E−07	1.83E−07	1.24E−07
^{37}Ar	2.80E−05	2.04E−05	1.42E−05
^{39}Ar	4.82E−08	1.06E−08	6.76E−09
^{40}K	4.73E−08	1.68E−08	1.06E−08
^{41}Ca	6.04E−06	4.03E−06	2.64E−06
^{44}Ti	1.18E−05	1.22E−05	1.18E−05
^{48}V	9.31E−08	6.77E−08	5.28E−08
^{49}V	4.56E−07	2.92E−07	2.29E−07
^{48}Cr	3.61E−04	3.80E−04	3.73E−04
^{49}Cr	2.36E−05	2.49E−05	2.33E−05
^{51}Cr	6.06E−06	5.58E−06	5.25E−06
^{51}Mn	8.61E−05	8.92E−05	8.15E−05
^{52}Mn	5.47E−06	5.12E−06	4.51E−06
^{53}Mn	2.14E−04	2.08E−04	2.00E−04
^{54}Mn	2.77E−06	2.83E−06	2.93E−06
^{52}Fe	9.11E−03	9.31E−03	9.00E−03
^{53}Fe	9.68E−04	9.73E−04	9.07E−04
^{55}Fe	1.88E−03	1.83E−03	1.76E−03
^{59}Fe	1.74E−06	2.77E−07	1.59E−07
^{60}Fe	9.91E−06	1.62E−06	8.55E−07
^{55}Co	1.10E−02	1.09E−02	1.01E−02
^{56}Co	1.27E−04	1.23E−04	1.13E−04
^{57}Co	9.06E−04	8.88E−04	8.58E−04
^{58}Co	4.27E−06	4.28E−06	4.38E−06
^{60}Co	4.18E−06	9.02E−07	4.54E−07
^{56}Ni	6.03E−01	7.01E−01	7.99E−01
^{57}Ni	1.53E−02	1.77E−02	2.03E−02
^{59}Ni	4.05E−04	4.08E−04	4.07E−04
^{63}Ni	3.26E−06	7.75E−07	4.80E−07
^{62}Zn	1.79E−04	3.04E−04	4.59E−04
^{65}Zn	1.39E−06	7.04E−07	5.03E−07
^{65}Ga	4.94E−08	7.95E−08	1.17E−07
^{68}Ge	4.14E−08	2.45E−08	1.86E−08

Table 4. Asymptotic nucleosynthetic yields of stable isotopes (in solar masses) for different DDT8_N100 models.

	rpc32	rpc40	c50
^{12}C	5.65E−03	1.50E−03	9.84E−04
^{13}C	1.01E−08	3.59E−09	2.50E−09
^{14}N	2.69E−06	5.94E−07	3.94E−07
^{15}N	3.18E−09	6.57E−10	4.21E−10
^{16}O	1.21E−01	5.52E−02	3.47E−02
^{17}O	4.88E−07	1.14E−07	7.61E−08
^{18}O	4.98E−09	8.15E−10	5.10E−10
^{19}F	5.51E−10	6.70E−11	3.46E−11
^{20}Ne	6.44E−03	1.54E−03	8.98E−04
^{21}Ne	3.61E−07	7.18E−08	4.57E−08
^{22}Ne	4.79E−05	9.72E−06	6.14E−06
^{23}Na	5.10E−05	1.15E−05	7.13E−06
^{24}Mg	1.91E−02	9.08E−03	6.02E−03
^{25}Mg	6.59E−05	1.67E−05	1.02E−05
^{26}Mg	8.37E−05	1.98E−05	1.24E−05
^{27}Al	7.31E−04	2.94E−04	1.86E−04
^{28}Si	2.59E−01	2.48E−01	2.06E−01
^{29}Si	7.47E−04	3.77E−04	2.57E−04
^{30}Si	1.29E−03	6.19E−04	4.18E−04
^{31}P	3.94E−04	2.11E−04	1.47E−04
^{32}S	1.15E−01	1.14E−01	9.44E−02
^{33}S	2.52E−04	1.67E−04	1.20E−04
^{34}S	1.80E−03	1.21E−03	8.79E−04
^{36}S	1.44E−07	4.31E−08	2.82E−08
^{35}Cl	1.27E−04	7.83E−05	5.44E−05
^{37}Cl	2.85E−05	2.06E−05	1.44E−05
^{36}Ar	2.04E−02	2.03E−02	1.73E−02
^{38}Ar	1.01E−03	6.98E−04	4.76E−04
^{40}Ar	5.52E−08	1.16E−08	7.30E−09
^{39}K	9.47E−05	6.32E−05	4.14E−05
^{41}K	6.07E−06	4.04E−06	2.64E−06
^{40}Ca	1.76E−02	1.76E−02	1.57E−02
^{42}Ca	2.72E−05	1.69E−05	1.04E−05
^{43}Ca	9.59E−08	3.45E−08	2.65E−08
^{44}Ca	1.19E−05	1.22E−05	1.18E−05
^{46}Ca	2.95E−08	5.29E−09	3.19E−09
^{48}Ca	2.93E−09	6.14E−10	3.97E−10
^{45}Sc	3.40E−07	1.96E−07	1.42E−07
^{46}Ti	1.49E−05	1.01E−05	6.67E−06
^{47}Ti	6.42E−07	4.60E−07	3.82E−07
^{48}Ti	3.62E−04	3.80E−04	3.73E−04
^{49}Ti	2.41E−05	2.52E−05	2.35E−05
^{50}Ti	3.12E−07	2.70E−07	2.55E−07
^{50}V	3.85E−08	1.39E−08	9.37E−09
^{51}V	9.28E−05	9.53E−05	8.73E−05
^{50}Cr	2.96E−04	3.02E−04	2.65E−04
^{52}Cr	9.66E−03	9.87E−03	9.58E−03
^{53}Cr	1.18E−03	1.18E−03	1.11E−03
^{54}Cr	1.08E−05	1.06E−05	1.05E−05
^{55}Mn	1.29E−02	1.27E−02	1.19E−02
^{54}Fe	9.90E−02	9.54E−02	8.52E−02
^{56}Fe	6.20E−01	7.19E−01	8.17E−01
^{57}Fe	1.62E−02	1.86E−02	2.11E−02
^{58}Fe	7.79E−05	7.55E−05	7.51E−05
^{59}Co	5.09E−04	5.66E−04	6.37E−04
^{58}Ni	6.27E−02	6.50E−02	6.64E−02
^{60}Ni	4.49E−03	5.11E−03	5.92E−03
^{61}Ni	5.33E−05	6.47E−05	9.08E−05
^{62}Ni	3.05E−04	3.99E−04	5.47E−04
^{64}Ni	2.53E−06	8.73E−07	5.89E−07
^{63}Cu	1.17E−05	4.27E−06	3.04E−06
^{65}Cu	4.28E−06	1.92E−06	1.41E−06
^{64}Zn	9.90E−06	7.06E−06	6.99E−06
^{66}Zn	1.34E−05	8.50E−06	7.61E−06
^{67}Zn	6.23E−07	2.03E−07	1.39E−07
^{68}Zn	7.56E−07	3.89E−07	2.79E−07
^{70}Zn	2.06E−08	6.41E−09	4.23E−09
^{69}Ga	4.16E−07	1.98E−07	1.42E−07
^{71}Ga	6.61E−08	2.77E−08	1.94E−08